



Opposite Trends in Holocene Speleothem Proxy Records From Two Neighboring Caves in Germany: A Multi-Proxy Evaluation

Michael Weber^{1,2*}, Yvonne Hinz¹, Bernd R. Schöne¹, Klaus Peter Jochum², Dirk Hoffmann³, Christoph Spötl⁴, Dana F. C. Riechelmann¹ and Denis Scholz¹

¹ Institute for Geosciences, Johannes Gutenberg University Mainz, Mainz, Germany, ² Climate Geochemistry Department, Max Planck Institute for Chemistry (Otto Hahn Institute), Mainz, Germany, ³ Isotope Geology Department, Georg-August-University Göttingen, Göttingen, Germany, ⁴ Institute of Geology, University of Innsbruck, Innsbruck, Austria

OPEN ACCESS

Edited by:

Eleonora Regattieri,
Pisa Research Area, Italian National
Research Council, Italy

Reviewed by:

Maša Surić,
University of Zadar, Croatia
Silvia Frisia,
University of New South Wales,
Australia

*Correspondence:

Michael Weber
michael.weber@uni-mainz.de

Specialty section:

This article was submitted to
Quaternary Science, Geomorphology,
and Paleoenvironment,
a section of the journal
Frontiers in Earth Science

Received: 16 December 2020

Accepted: 22 February 2021

Published: 12 March 2021

Citation:

Weber M, Hinz Y, Schöne BR,
Jochum KP, Hoffmann D, Spötl C,
Riechelmann DFC and Scholz D
(2021) Opposite Trends in Holocene
Speleothem Proxy Records From Two
Neighboring Caves in Germany:
A Multi-Proxy Evaluation.
Front. Earth Sci. 9:642651.
doi: 10.3389/feart.2021.642651

Holocene climate in Central Europe was characterized by variations on millennial to decadal time scales. Speleothems provide the opportunity to study such palaeoclimate variability using high temporal resolution proxy records, and offer precise age models by U-series dating. However, the significance of proxy records from an individual speleothem is still a matter of debate, and limited sample availability often hampers the possibility to reproduce proxy records or to resolve spatial climate patterns. Here we present a palaeoclimate record based on four stalagmites from the Hüttenbläuserschachthöhle (HBSH), western Germany. Two specimens cover almost the entire Holocene, with a short hiatus in between. A third stalagmite grew between 6.1 ± 0.6 ka and 0.6 ± 0.1 ka and a fourth one covers 11.0 ± 0.4 ka to 8.2 ± 0.2 ka. Trace element and stable isotope data allow to compare coeval stalagmites and to reconstruct potential climate patterns in the Holocene. In addition, Sr isotopes reveal soil processes and recharge of the aquifer. The aim of this study was to evaluate the consistency of the proxy data recorded by the individual stalagmites and to validate the results using a multi-proxy approach. Due to the close proximity of HBSH (<1 km) to the intensively investigated Bunker Cave system, this dataset also provides the unique opportunity to compare this record with a time-series from another cave system in the same climate region. While the initial growth phase at the onset of the Holocene shows similar patterns in both caves, the data show an opposing trend in the past 6 ka, most likely induced by the effect of disequilibrium isotope fractionation, resulting in a strong increase in $\delta^{13}\text{C}$ and $\delta^{18}\text{O}$ values. The stable isotope data from Bunker Cave do not show this pattern. Trace element data support the interpretation of the HBSH stable isotope data, highlighting the importance of a multi-proxy approach, and the need to replicate speleothem records both within a cave system and ideally using other caves in the region.

Keywords: stalagmite, PCP, Sr isotopes, Central Europe, stable isotopes, disequilibrium isotope effects, trace elements

INTRODUCTION

Speleothems are well established terrestrial palaeoclimate archives and widely used for the reconstruction of past climate and environmental variability on different time scales (e.g., Genty et al., 2003; Fohlmeister et al., 2012; Moseley et al., 2014; Luetscher et al., 2015; Wassenburg et al., 2016a; Mischel et al., 2017a; Lechleitner et al., 2018; Weber et al., 2018a; Budsky et al., 2019). One of their key features is the possibility to obtain independent, precise and accurate ages, using the U-series disequilibrium method (Scholz and Hoffmann, 2008; Cheng et al., 2013) and the construction of a robust age-depth model, provided that post-depositional alteration did not affect U-mobilization (Scholz et al., 2014; Bajo et al., 2016). The most commonly used climate proxies in speleothem science are the stable oxygen ($\delta^{18}\text{O}$) and carbon ($\delta^{13}\text{C}$) isotopes as well as trace elements (McDermott, 2004; Fairchild et al., 2006; Fairchild and Treble, 2009; Lachniet, 2009). Both can be measured at high spatial resolution in the sub-100 μm -range and converted into a temporally aligned dataset using an age-depth model (e.g., Scholz and Hoffmann, 2011; Breitenbach et al., 2012). Trace elements can be analyzed at similar or even higher resolution and have been extensively used in speleothem science to further constrain environmental and climate reconstructions (e.g., Fairchild et al., 2000; Treble et al., 2003; Fairchild and Treble, 2009; Sinclair et al., 2012). Furthermore, additional proxies have been established for speleothems, such as Sr isotopes to reconstruct changes in aeolian dust transport, weathering conditions, precipitation amount, and water pathways in the karst aquifer (e.g., Banner et al., 1994, 1996; Li et al., 2005; Hori et al., 2013; Belli et al., 2017; Weber et al., 2017, 2018a).

Although all these proxies – and in particular stable oxygen and carbon isotopes – have been intensively studied, the reconstruction of past climate variability can be hampered by several processes. Besides the natural variability of $\delta^{18}\text{O}$ and $\delta^{13}\text{C}$ values reflecting climatic and environmental changes, karst and in-cave processes can also significantly alter the resulting proxy signal captured by the speleothem (e.g., Mickler et al., 2006; Lachniet, 2009; Deininger et al., 2012; Riechelmann et al., 2013; Hansen et al., 2017, 2019). Therefore, it is important to evaluate the significance of a stable isotope record obtained from a single speleothem, either by using a multi-proxy approach to validate the stable isotope data, or, if available, by analyzing several speleothems from the same time interval and cave system. This is especially crucial for time intervals of sparse speleothem growth, e.g., during Marine Isotope Stage 3 in Central Europe (McDermott, 2004; Fankhauser et al., 2016; Weber et al., 2018a), and when additional samples are not available. In contrast to time intervals with a low number of speleothem records, the favorable climatic conditions during the Holocene resulted in intensive speleothem growth (e.g., McDermott et al., 1999; Mangini et al., 2007; Fohlmeister et al., 2012, 2013; Warken et al., 2018; Comas-Bru et al., 2020), providing the largest possible cross-continental dataset to evaluate the significance of speleothem proxy records.

Although Holocene climate variability is much smaller compared to glacial-interglacial timescales (Mayewski et al., 2004; McDermott, 2004; Wanner et al., 2008), significant changes

and trends in precipitation and temperature also occurred during the Holocene. Here, speleothem proxy data from Hüttenbläuserschachthöhle (HBSH), western Germany, covering almost the entire Holocene is presented. In total, four stalagmites were investigated and their $\delta^{18}\text{O}$ and $\delta^{13}\text{C}$ values analyzed. These records were stacked and their significance evaluated by comparing them with published data from the nearby Bunker cave (<1 km distance to Hüttenbläuserschachthöhle). To further evaluate the stable isotope data, a multi-proxy approach including trace element and Sr isotope data was used.

SITE AND SAMPLE DESCRIPTION

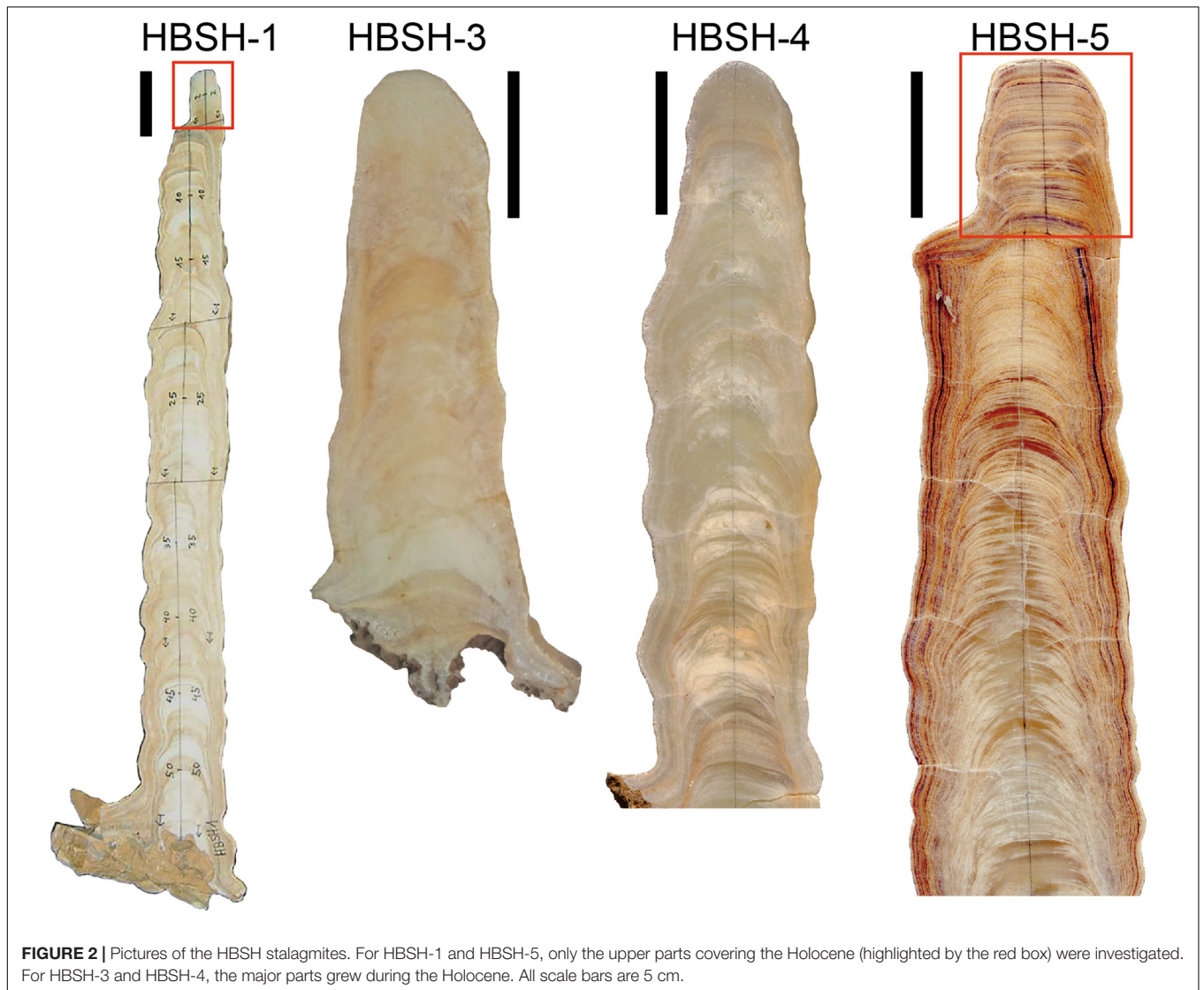
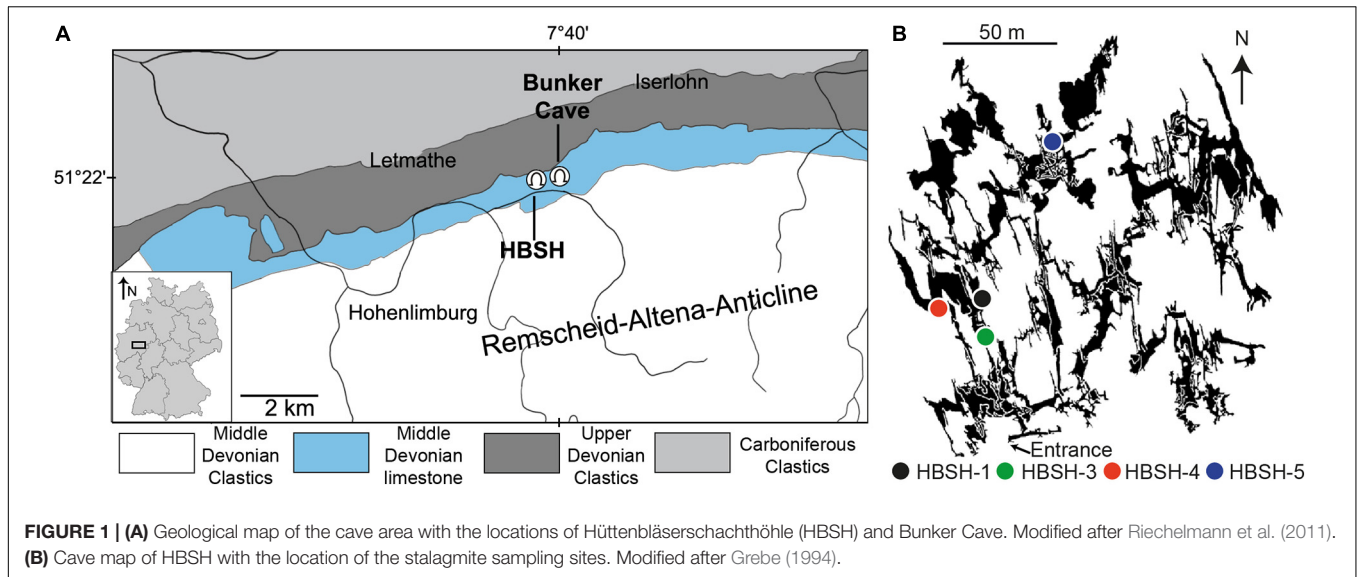
Hüttenbläuserschachthöhle (HBSH)

Hüttenbläuserschachthöhle (HBSH in the following) is located within upper Middle Devonian limestones (Givetian stage) of the northern Rhenish Slate Mountains (Iserlohn-Letmathe, NW Germany, **Figure 1A** (Burchette, 1981). Ridges and valleys in the area of Iserlohn-Letmathe generally follow the WSW-ENE strike of the rock formation (von Kamp and Ribbert, 2005). The approximately 700 m thick limestone was deposited in a shallow shelf (Paeckelmann, 1922; Krebs, 1974). At the transition between the Givetian and the Frasnian, basin subsidence and sea-level rise exceeded carbonate sedimentation, giving rise to siliciclastic depositions in deeper water depths (Hammerschmidt et al., 1995).

Hüttenbläuserschachthöhle was discovered in 1993 and is one of the largest and speleothem-richest caves in Iserlohn-Letmathe (Hammerschmidt et al., 1995; Richter et al., 2015). The cave has a total length of 4.8 km with a vertical extent of 46 m (Grebe, 1994) and consists of three levels. On each level, a main corridor exists, which probably represents the former phreatic karst water collector. The cave levels can be correlated to river terraces in the Rhenish Slate Mountains (Niggemann et al., 2003). The area above HBSH and the nearby Bunker Cave is covered by similar vegetation consisting of C3-plants such as ash, beech trees and shrubs. The mean annual precipitation is 972 ± 173 mm (1 SD, 1978–2020) and the mean annual temperature in the area is $8.9 \pm 0.7^\circ\text{C}$ (1 SD; 1994–2020, DWD weather station Lüdenscheid, approximately 15 km south of HBSH). The $\delta^{18}\text{O}$ values of precipitation range from -5 ‰ in summer to -13 ‰ in winter and averages -8.0 ‰ between 2006 and 2013 (Riechelmann et al., 2017).

Speleothem Samples

The four stalagmites covering the Holocene (HBSH-1, HBSH-3, HBSH-4, and HBSH-5, **Figure 2**) were collected from deep parts of HBSH. HBSH-1 is a ca. 55 cm-long stalagmite with clearly visible macroscopic banding. X-ray diffraction revealed that most of the sample consist of aragonite, with very few and short calcite sections (Jochum et al., 2012; Yang et al., 2015; Lin et al., 2017). This study focuses on an approximately 5 cm-long section from the top of the stalagmite. In contrast to HBSH-1, all other stalagmites of this study consist of calcite. HBSH-3 is approximately 22 cm long, banded and bright beige colored with some interspersed darker areas. HBSH-4 also



shows banding throughout the whole stalagmite, which measures 30 cm in length, with a bright beige to gray color. HBSH-5 has a total length of 33 cm, showing macroscopic banding and a generally darker color than the other HBSH stalagmites. While stalagmites HBSH-1, -3, and -4 grew in close proximity in the western part of HBSH, HBSH-5 was sampled in the norther part of HBSH (Figure 1B). This area is only sparsely decorated with speleothem deposits, potentially related to limited fractures in the overlying host rock (Hammerschmidt et al., 1995). The top section of HBSH-5 covering approximately 6 cm was investigated in this study.

ANALYTICAL METHODS

$^{230}\text{Th}/\text{U}$ -Dating

Stalagmite samples were dated using the $^{230}\text{Th}/\text{U}$ dating method and analyzed by multi-collector inductively coupled plasma mass spectrometry (MC-ICP-MS) at the Max Planck Institute for Chemistry (MPIC), Mainz, the Institute for Geosciences, Mainz, and the Bristol Isotope Group (BIG), Bristol (HBSH-1). Samples were cut along the growth axes using a diamond wire saw. In total, 47 samples were analyzed at MPIC, seven samples at the Institute for Geosciences, Mainz, and five samples at BIG (Table 1). For sample HBSH-3, HBSH-4, and HBSH-5, sample amounts of approximately 300 mg were used, and chemical separation of U and Th prior to analysis was performed at the MPIC and the Institute for Geosciences following the methods described in Hoffmann (2008) and Yang et al. (2015). Chemical separation for HBSH-1 was performed at BIG as described by Hoffmann et al. (2007). At MPIC, a Nu Plasma MC-ICP-MS was used to analyze U and Th in separated sessions following the protocol described in Obert et al. (2016). Details of the calibration of the U-Th-spike are presented by Gibert et al. (2016). Introduction of the samples dissolved in 0.8 mol/L HNO_3 was performed using a CETAC Aridus II desolvating nebulizer system. A daily tuning protocol was used to achieve highest signal intensities and optimized peak shapes. At the Institute for Geosciences, a Neptune Plus MC-ICP-MS was coupled to a CETAC Aridus 3 desolvating nebulizer system, performing the same protocol as described for the Nu Plasma at MPIC. Measurements at BIG were performed using a Neptune MC-ICP-MS coupled to a CETAC Aridus desolvating system, following the methods described in Hoffmann et al. (2007). Age-depth models (Figure 3) were calculated using the algorithm StalAge (Scholz and Hoffmann, 2011).

Stable Isotope Analysis

Stable carbon and oxygen isotope values ($\delta^{13}\text{C}$ and $\delta^{18}\text{O}$) for HBSH-3, HBSH-4, and HBSH-5 were determined at the Institute for Geosciences, Johannes Gutenberg University Mainz. Samples were obtained with a semi-automated drilling device at a spatial resolution of 500 μm . In total, 1350 samples were analyzed using a Thermo Fisher Scientific MAT 253 continuous-flow isotope ratio mass spectrometer equipped with a Gasbench II. Stable carbon and oxygen isotope values for HBSH-1 were obtained at the Institute of Geology, University of Innsbruck, using a Merchantek video-controlled Micromill

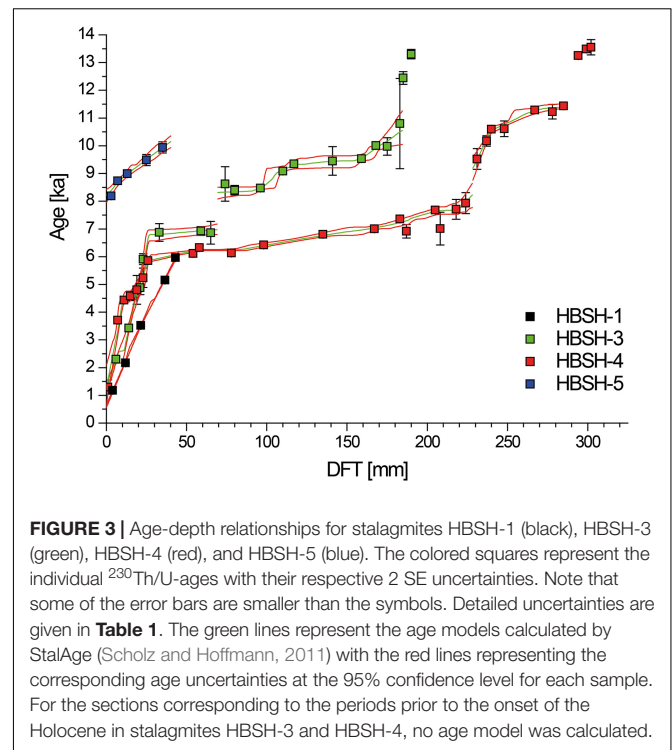


FIGURE 3 | Age-depth relationships for stalagmites HBSH-1 (black), HBSH-3 (green), HBSH-4 (red), and HBSH-5 (blue). The colored squares represent the individual $^{230}\text{Th}/\text{U}$ -ages with their respective 2 SE uncertainties. Note that some of the error bars are smaller than the symbols. Detailed uncertainties are given in Table 1. The green lines represent the age models calculated by StalAge (Scholz and Hoffmann, 2011) with the red lines representing the corresponding age uncertainties at the 95% confidence level for each sample. For the sections corresponding to the periods prior to the onset of the Holocene in stalagmites HBSH-3 and HBSH-4, no age model was calculated.

device (Dettman and Lohmann, 1995) at a spatial resolution of 150 μm , resulting in a total number of 301 samples. Analyses were performed using a Thermo Fisher Scientific Delta^{plus}XL isotope ratio mass spectrometer linked to a Gasbench II. Analytical precision and accuracy at the 1 σ -level was better than 0.08 ‰ for $\delta^{13}\text{C}$ and $\delta^{18}\text{O}$. All values are reported relative to V-PDB.

Trace Element Analyses

Laser ablation inductively coupled plasma mass spectrometry (LA-ICP-MS) was used to determine trace element concentrations in HBSH-1, HBSH-3, and HBSH-5. A Thermo Fisher Scientific Element 2 SF-ICP-MS was coupled to a New Wave UP-213 laser ablation system at the MPIC. For all samples, the following laser parameters were applied: spot analyses with a spot size of 100 μm , a repetition rate of 10 Hz and an energy output of 60%, resulting in a fluence of $\approx 5 \text{ J}/\text{cm}^2$. Background signals were collected for 14 s prior to ablation and subtracted from the sample signal, followed by a wash-out time of 20 s. The following analytes were measured during the session: ^{25}Mg , ^{31}P , ^{88}Sr , and ^{137}Ba . NIST SRM 612 was analyzed for calibration purposes at the beginning, between each set and at the end of the routine. ^{43}Ca was used as internal reference to calculate trace element concentrations. Data evaluation was performed offline, following the calculations presented in Mischel et al. (2017b).

Data Processing and Statistics

All speleothems show a high variability in growth rate, both within individual stalagmites and between coeval stalagmites

TABLE 1 | Uranium and Th concentrations, activity ratios and $^{230}\text{Th}/\text{U}$ -ages for the Holocene stalagmites from HBSH. All uncertainties are quoted as 2 SE. All activity ratios and ages were corrected for detrital contamination assuming a $^{232}\text{Th}/^{238}\text{U}$ mass ratio of 3.8 ± 1.9 , calculated from the average Th and U concentrations of tonalities which are believed to be representative for the bulk continental crust (Wedepohl, 1995). ^{230}Th , ^{234}U , and ^{238}U were assumed to be in secular equilibrium for the detritus. Activity ratios were calculated using the half-lives from Cheng et al. (2000). All measurements highlighted with an asterisk were measured at the Institute for Geosciences with a Neptune Plus MC-ICP-MS. Sample HBSH-1 was analyzed at the BIG. BDL = below detection limit; NA = not available due to ^{232}Th concentration below detection limit. All ages are given relative to the year AD 2000.

Sample	DFT [mm]	^{232}Th [ng/g]	Uncertainty	^{238}U [ng/g]	Uncertainty	$(^{234}\text{U}/^{238}\text{U})$ Uncertainty	$(^{230}\text{Th}/^{238}\text{U})$ Uncertainty	$(^{232}\text{Th}/^{238}\text{U})$ Uncertainty	Uncorrected age [ka]	Uncertainty [ka]	Corrected Age [ka]	Uncertainty [ka]			
HBSH-1-0.4	4.0	2.167	0.284	2727.52	364.02	1.965	0.003	0.0211	0.0002	81.9	0.5	1.18	0.01	1.17	0.01
HBSH-1-1.2	12.0	2.543	0.290	3427.39	392.00	2.142	0.003	0.0421	0.0002	174.3	0.9	2.17	0.01	2.16	0.01
HBSH-1-2.2	21.5	0.690	0.086	6186.75	773.74	1.891	0.003	0.0601	0.0003	1647.7	12.0	3.51	0.02	3.51	0.02
HBSH-1-3.7	36.5	4.109	0.320	4876.50	372.62	1.932	0.003	0.0895	0.0004	325.2	2.1	5.16	0.03	5.15	0.03
HBSH-1-4.3	43.0	34.837	2.624	4219.61	315.69	1.838	0.003	0.0981	0.0011	37.1	0.1	6.09	0.03	5.96	0.07
HBSH-3-0.2	2.0	0.906	0.055	38.54	0.48	1.228	0.014	0.0411	0.0145	6.1	1.9	4.26	1.33	3.70	1.34
HBSH-3-0.6	6.0	0.453	0.005	72.30	0.43	1.211	0.002	0.0253	0.0011	13.1	0.4	2.44	0.07	2.29	0.10
HBSH-3-1.4	14.0	0.066	0.001	38.05	0.25	1.208	0.002	0.0373	0.0011	66.6	2.1	3.46	0.10	3.41	0.11
HBSH-3-2.1	21.0	1.540	0.015	80.34	0.49	1.204	0.003	0.0527	0.0026	9.2	0.2	5.32	0.09	4.87	0.25
HBSH-3-2.3	23.0	0.789	0.014	99.27	0.79	1.208	0.008	0.0638	0.0021	25.3	0.8	6.09	0.18	5.90	0.20
HBSH-3-3.3	33.0	0.864	0.009	43.21	0.29	1.205	0.002	0.0737	0.0033	12.0	0.4	7.34	0.22	6.86	0.32
HBSH-3-5.9	59.0	0.413	0.005	45.97	0.31	1.212	0.002	0.0746	0.0016	26.1	0.5	7.12	0.12	6.91	0.16
HBSH-3-6.5*	65.0	6.530	0.043	87.64	0.52	1.226	0.002	0.0748	0.0044	3.8	0.1	8.60	0.15	6.85	0.41
HBSH-3-7.4	74.0	2.670	0.029	91.33	0.55	1.249	0.003	0.0951	0.0067	11.4	0.2	9.96	0.21	8.61	0.62
HBSH-3-8.0	80.0	0.096	0.001	51.95	0.35	1.249	0.002	0.0926	0.0018	153.8	3.4	8.42	0.17	8.38	0.17
HBSH-3-9.6	96.0	0.030	0.000	63.08	0.42	1.252	0.002	0.0937	0.0008	603.0	9.6	8.48	0.08	8.46	0.08
HBSH-3-11.0	110.0	0.432	0.005	109.01	0.85	1.259	0.007	0.1008	0.0013	78.5	1.1	9.17	0.13	9.08	0.13
HBSH-3-11.7	117.0	0.299	0.004	121.87	0.72	1.266	0.002	0.1041	0.0014	130.7	2.2	9.39	0.13	9.34	0.14
HBSH-3-14.1	141.0	0.111	0.005	93.56	1.96	1.278	0.026	0.1062	0.0051	273.8	17.1	9.47	0.51	9.44	0.52
HBSH-3-15.9	159.0	0.056	0.001	67.35	0.45	1.266	0.002	0.1061	0.0012	394.0	6.3	9.54	0.11	9.52	0.11
HBSH-3-16.8	168.0	0.007	0.000	52.59	0.36	1.263	0.002	0.1109	0.0012	2597.0	77.8	10.00	0.11	9.99	0.11
HBSH-3-17.5*	175.0	3.980	0.030	68.82	0.45	1.318	0.002	0.1155	0.0035	6.8	0.1	11.22	0.15	9.96	0.31
HBSH-3-18.3	183.0	13.302	0.132	88.41	0.69	1.343	0.011	0.1270	0.0182	3.3	0.1	14.06	0.26	10.79	1.63
HBSH-3-18.5*	185.0	6.838	0.048	156.76	0.99	1.369	0.001	0.1481	0.0025	11.1	0.1	13.34	0.11	12.42	0.23
HBSH-3-19.0	190.0	1.162	0.014	87.29	0.63	1.382	0.002	0.1593	0.0019	37.3	0.4	13.56	0.11	13.29	0.17
HBSH-4-0.1	1.0	1.859	0.019	91.22	0.52	1.209	0.002	0.0143	0.0028	2.9	0.1	1.77	0.07	1.29	0.26
HBSH-4-0.7	7.0	1.198	0.012	158.11	1.07	1.208	0.005	0.0404	0.0012	17.1	0.3	3.88	0.08	3.70	0.12
HBSH-4-1.1	11.0	1.117	0.012	192.76	1.18	1.179	0.002	0.0469	0.0009	25.5	0.3	4.56	0.05	4.42	0.08
HBSH-4-1.5	15.0	0.205	0.004	243.41	1.47	1.180	0.002	0.0486	0.0018	177.4	7.2	4.59	0.17	4.57	0.17

(Continued)

TABLE 1 | Continued

Sample	DFT [mm]	²³² Th [ng/g]	Uncertainty	²³⁸ U [ng/g]	Uncertainty	(²³⁴ U / ²³⁸ U)	Uncertainty	(²³⁰ Th / ²³⁸ U)	Uncertainty	(²³² Th / ²³² Th)	Uncertainty	Uncorrected age [ka]	Uncertainty [ka]	Corrected Age [ka]	Uncertainty [ka]
HBSH-4-1.9	19.0	7.369	0.073	173.13	0.98	1.181	0.002	0.0509	0.0054	4.4	0.1	5.83	0.07	4.79	0.52
HBSH-4-2.3*	23.0	8.998	0.064	143.71	0.91	1.185	0.001	0.0556	0.0037	3.5	0.0	6.75	0.09	5.22	0.35
HBSH-4-2.6	26.0	0.400	0.004	236.87	1.45	1.171	0.002	0.0612	0.0007	111.7	1.5	5.89	0.06	5.85	0.07
HBSH-4-5.4	54.0	0.131	0.002	268.41	1.57	1.132	0.002	0.0618	0.0010	386.8	7.6	6.12	0.10	6.11	0.10
HBSH-4-5.8	58.0	0.205	0.003	262.36	1.62	1.129	0.002	0.0636	0.0008	250.1	4.1	6.33	0.08	6.31	0.08
HBSH-4-7.8	78.0	0.231	0.003	288.26	1.72	1.160	0.002	0.0643	0.0010	246.3	4.8	6.22	0.10	6.12	0.10
HBSH-4-9.8	98.0	0.163	0.002	276.67	1.70	1.160	0.002	0.0664	0.0008	346.1	5.7	6.43	0.08	6.41	0.08
HBSH-4-13.5	135.0	0.093	0.001	328.15	1.89	1.157	0.002	0.0700	0.0007	758.0	10.2	6.81	0.07	6.80	0.07
HBSH-4-16.7	167.0	0.000	0.001	303.52	1.84	1.159	0.002	0.0721	0.0008	173071.5	472258.2	6.99	0.08	6.99	0.08
HBSH-4-18.3	183.0	1.506	0.015	302.81	1.75	1.138	0.002	0.0742	0.0008	46.4	0.5	7.47	0.06	7.34	0.08
HBSH-4-18.7	187.0	3.763	0.050	281.12	1.60	1.134	0.002	0.0697	0.0024	16.7	0.4	7.24	0.17	6.90	0.24
HBSH-4-20.5	205.0	1.045	0.011	296.24	2.11	1.155	0.005	0.0785	0.0009	68.8	0.9	7.75	0.09	7.67	0.10
HBSH-4-20.8	208.0	13.369	0.132	281.26	1.61	1.156	0.002	0.0720	0.0060	5.4	0.1	8.19	0.10	7.00	0.59
HBSH-4-21.8	218.0	5.615	0.055	200.84	1.14	1.155	0.002	0.0788	0.0035	9.4	0.1	8.39	0.08	7.70	0.36
HBSH-4-22.4*	224.0	12.987	0.089	191.34	1.20	1.187	0.001	0.0833	0.0038	4.5	0.0	9.57	0.08	7.91	0.38
HBSH-4-23.1	231.0	7.632	0.076	245.08	1.41	1.182	0.002	0.0989	0.0038	10.4	0.1	10.27	0.08	9.51	0.37
HBSH-4-23.7	237.0	3.146	0.032	242.88	1.47	1.155	0.003	0.1029	0.0017	25.0	0.3	10.48	0.09	10.16	0.19
HBSH-4-24.0	240.0	1.048	0.011	307.01	1.85	1.177	0.002	0.1091	0.0009	98.4	1.1	10.66	0.09	10.58	0.09
HBSH-4-24.8*	248.0	BDL	BDL	281.40	1.79	1.180	0.001	0.1096	0.0028	NA	NA	10.59	0.28	10.59	0.28
HBSH-4-26.7	267.0	2.244	0.023	306.56	1.89	1.206	0.002	0.1187	0.0012	50.3	0.5	11.45	0.09	11.27	0.12
HBSH-4-27.8	278.0	0.356	0.010	298.43	1.84	1.204	0.002	0.1180	0.0025	303.4	10.7	11.27	0.26	11.22	0.26
HBSH-4-28.5*	285.0	0.613	0.005	292.35	1.84	1.208	0.001	0.1205	0.0008	176.2	1.4	11.47	0.07	11.42	0.08
HBSH-4-29.4	294.0	0.918	0.010	291.94	1.92	1.217	0.004	0.1395	0.0011	136.4	1.5	13.31	0.11	13.24	0.12
HBSH-4-29.9	299.0	1.340	0.013	318.18	1.85	1.222	0.002	0.1425	0.0010	104.2	1.0	13.57	0.09	13.48	0.10
HBSH-4-30.2	302.0	7.717	0.076	359.05	2.08	1.228	0.002	0.1438	0.0027	21.2	0.2	14.04	0.13	13.54	0.28
HBSH-5-0.3	3.0	2.162	0.021	172.21	1.18	3.042	0.013	0.2216	0.0021	54.6	0.5	8.30	0.07	8.18	0.09
HBSH-5-0.7	7.0	5.670	0.057	205.14	1.20	3.283	0.009	0.2544	0.0032	28.7	0.3	8.96	0.06	8.72	0.12
HBSH-5-1.3	13.0	1.708	0.023	68.17	0.45	3.324	0.009	0.2650	0.0037	32.9	0.5	9.19	0.10	8.98	0.13
HBSH-5-2.5	25.0	7.054	0.114	211.18	1.30	3.320	0.014	0.2788	0.0056	26.1	0.6	9.76	0.16	9.47	0.21
HBSH-5-3.5	35.0	32.228	0.559	2196.37	16.80	3.342	0.015	0.2936	0.0055	61.8	1.5	10.05	0.19	9.89	0.25

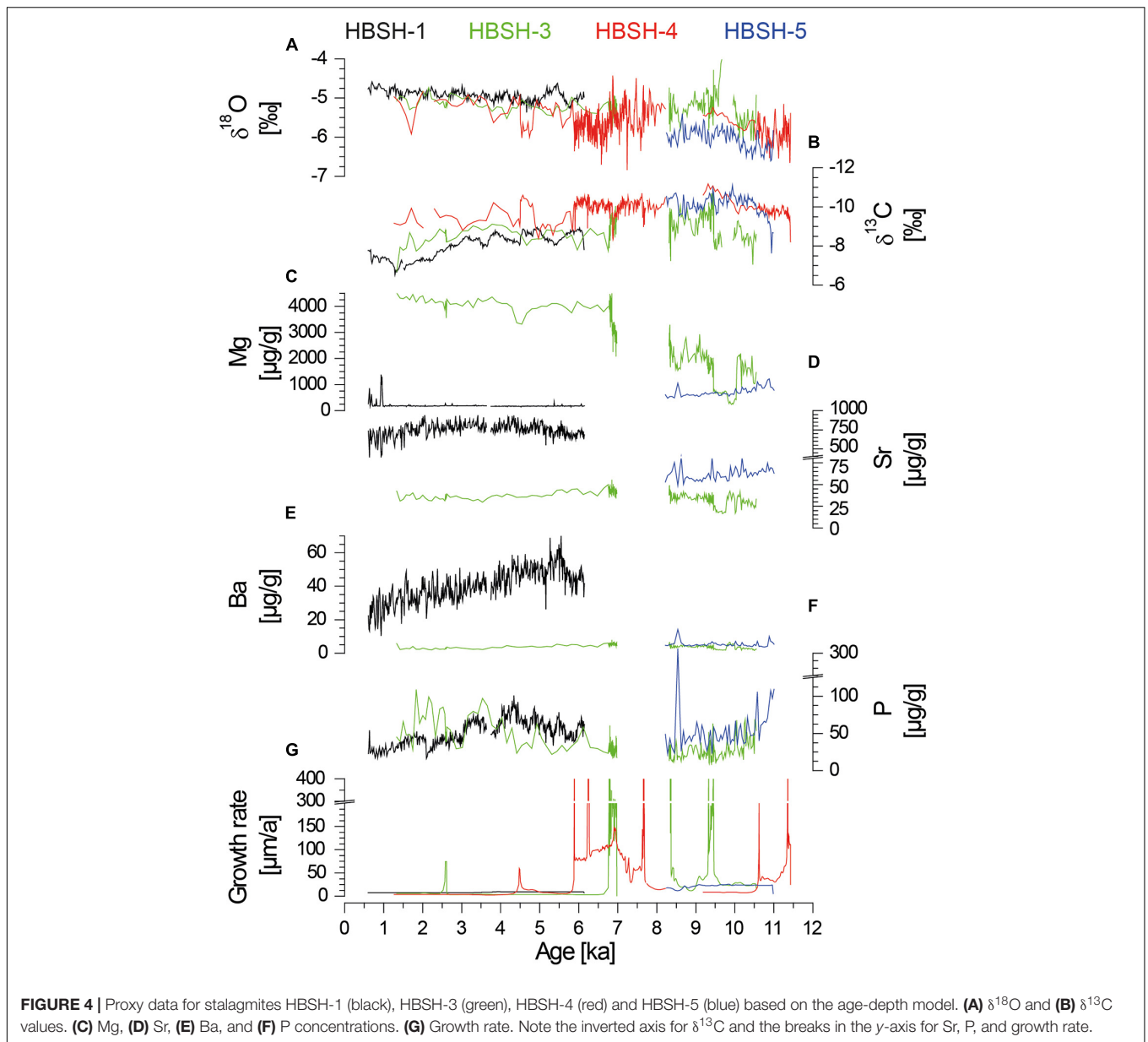
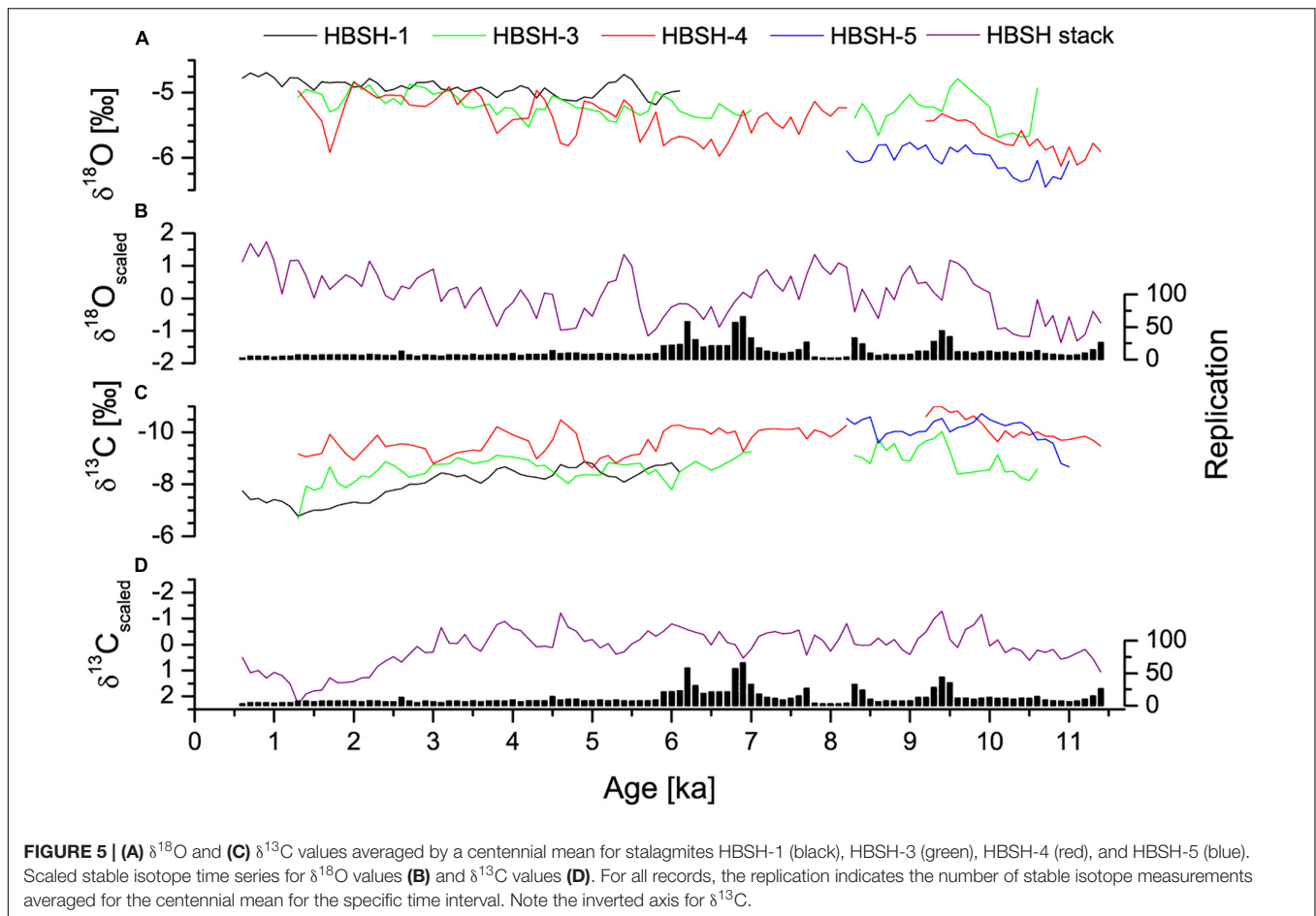


(Figure 4 and Supplementary Figure A4). Therefore, the stable isotope and trace element data shows high variability in temporal resolution. The aim of this study is to identify common long-term trends in the proxy records of the different samples, independent of the absolute $\delta^{13}\text{C}$ and $\delta^{18}\text{O}$ values, as well as trace element concentrations. To overcome potential biases due to differences in age resolution, centennial means for the stable isotope and trace element data were calculated. This is also a basic requirement for regression analysis (see sections “Within-cave correlation of speleothem records from HBSH and Bunker Cave” and “Inter-cave correlation of speleothem records from HBSH and Bunker Cave”), which was performed with the centennial stable isotope data using the statistical software R (R Core Team, 2020). The stalagmite samples differ in their mineralogy (i.e., aragonite and calcite) as well as growth rate and absolute $\delta^{13}\text{C}$ and $\delta^{18}\text{O}$ values. These differences can cause

steps in the stacked isotope time series, which is particularly important for intervals of low replication, and if only a single stalagmite is available for a specific time interval. To avoid steps in the final dataset (Figures 4, 5), a composite stack for HBSH (Figure 5) was constructed using scaled stable isotope data of each speleothem. Scaling was performed using the “scale()” function of the statistical software R (R Core Team, 2020) and refers to subtraction of the mean and division by the standard deviation for each time series. Due to the scaling, differences in absolute $\delta^{13}\text{C}$ and $\delta^{18}\text{O}$ values can be neglected. After calculating the scaled stable isotope data for each stalagmite, a composite stack was constructed using the previously calculated centennial means of all HBSH stalagmites. The number of individual analyses, which were arithmetically averaged for each mean value (replication), are also provided. These calculations were not only performed for HBSH, but also for the stable isotope values from



stalagmites from Bunker Cave covering the same time interval (Fohlmeister et al., 2012). Principal component analysis (PCA) was performed with the centennial means for stable isotope and trace elements and the “fviz_pca_biplot()” function of the statistical software R (R Core Team, 2020) and centennial means were calculated for stable isotopes and trace elements. To test the suitability of our dataset for PCAs and justify this approach, the Kaiser-Meyer-Olkin test for sampling adequacy (>0.5 ; Kaiser, 1970; Kaiser and Rice, 1974) and Bartlett’s test of sphericity (<0.05 ; Bartlett, 1937) were employed. Sample HBSH-5 did not pass the Kaiser-Meyer-Olkin test. Only principal components (PCs) with a standard deviation > 1.0 were considered and a cut-off value of 0.4 was chosen to describe the most important parameters of the PCA (Budaev, 2010). Detailed results including eigenvalues and factor loadings are presented in **Supplementary Table A1**. To evaluate the relationship between trace element and stable isotope data, a correlation analysis was performed using the statistical software R (R Core Team, 2020).

Strontium Isotope Analyses

Strontium isotope ratios ($^{87}\text{Sr}/^{86}\text{Sr}$) were determined for speleothem samples HBSH-3 ($n = 9$), HBSH-4 ($n = 9$), and HBSH-5 ($n = 3$). The samples (2 – 7 mg) were processed at the Institute for Geosciences, using a laminar flow hood in a clean

laboratory, following the methods described by Lugli et al. (2017) and Weber et al. (2018b) for dissolution and separation of Sr using Sr-spec resin. $^{87}\text{Sr}/^{86}\text{Sr}$ ratios were determined at the MPIC using a Nu Plasma MC-ICP-MS coupled to a CETAC Aridus II desolvating nebulizing system following the methods described by Weber et al. (2017). Ion beams were simultaneously collected using seven Faraday cups covering the m/z range of 82 – 88, representing the following isotopes: ^{82}Kr , ^{83}Kr , ^{84}Sr , ^{85}Rb , ^{86}Sr , ^{87}Sr , and ^{88}Sr . Strontium solutions were diluted to approximately 50 $\mu\text{g}/\text{mL}$ and measured in a standard-bracketing sequence, correcting for a NIST SRM 987 $^{87}\text{Sr}/^{86}\text{Sr}$ ratio of 0.710248 (McArthur et al., 2001). Correction for instrumental mass bias was performed using an exponential law, using a $^{88}\text{Sr}/^{86}\text{Sr}$ ratio of 8.375209 (Steiger and Jäger, 1977).

RESULTS

$^{230}\text{Th}/\text{U}$ -Dating

Results of the $^{230}\text{Th}/\text{U}$ -dating are presented in **Table 1**. Resulting age-depth models of all speleothem samples are presented in **Figure 3**, and all following ages refer to the age models resulting from StalAge (Scholz and Hoffmann, 2011). The studied section of speleothem HBSH-1 shows slow continuous growth between

6.1 ± 0.6 ka and 0.60 ± 0.06 ka with a stable growth rate of 8 μm/a (calculated based on the age-depth model). Sample HBSH-3 shows a more complex growth history. Two measurements yielded ages of 13.3 ± 0.2 ka and 12.4 ± 0.2 ka corresponding to the Bølling-Allerød. These ages were not included in the age model. Growth during the Holocene started at 10.8 ± 1.6 ka and continued at least until 8.3 ± 0.2 ka with the fastest growth rate (>100 μm/a) between 9.5 and 9.0 ka. A growth stop between 8.3 ± 0.2 ka and 7.0 ± 0.2 ka is indicated by the age-depth model and is followed by a phase of slow growth (6 μm/a) until the final stop at 1.3 ± 0.2 ka. The growth history of speleothem HBSH-4 is similar to HBSH-3 with an initial growth phase during the Bølling-Allerød between 13.6 ± 0.3 ka and 13.2 ± 0.1 ka, followed by a growth stop until 11.4 ± 0.1 ka, representing a growth inception shortly after the onset of the Holocene at 11.7 ± 0.1 ka. The initial growth phase for HBSH-4 lasted until 9.2 ± 0.4 ka and shows a deceleration from >30 μm/a to <10 μm/a toward a hiatus. Growth resumed around 8.2 ± 0.4 ka, and fast continuous growth (60 – 100 μm/a) is observed until 5.8 ± 0.1 ka, where a distinct growth deceleration (<10 μm/a) occurred, lasting until at least 3.7 ± 0.1 ka. The youngest age obtained from HBSH-4 is 1.3 ± 0.3 ka, and a continuous growth of approximately 3 μm/a until then is assumed. Speleothem HBSH-5 shows continuous growth between 9.9 ± 0.3 ka and 8.2 ± 0.1 ka and a rather constant growth rate of ≈20 μm/a for most of the studied part of the specimen. Only the youngest part shows a decelerating growth rate down to ≈10 μm/a between 8.7 ± 0.1 ka and 8.2 ± 0.1 ka.

Trace Elements

Trace element records of HBSH-1, -3, and -5 of Mg, P, Sr and Ba are presented in **Figure 4** and **Supplementary Figures A1–A3**.

Since HBSH-1 consists of aragonite (in contrast to the calcite speleothems HBSH-3 and HBSH-5), its trace element concentrations differ significantly from those of the other stalagmites (c.p., Wassenburg et al., 2016b). Magnesium in HBSH-1 is low (≈180 μg/g) for major parts of the sample except for some spikes, during the most recent 1000 years. For the whole growth phase, no general increasing or decreasing trend in Mg is visible. The Sr concentration is relatively high in comparison to the calcite speleothems, increasing from 500 to 800 μg/g towards more recent ages until 3.5 ± 0.1 ka. Afterward, this trend is reversed. The same pattern is visible in P, while Ba decreases on a longer time scale toward younger ages.

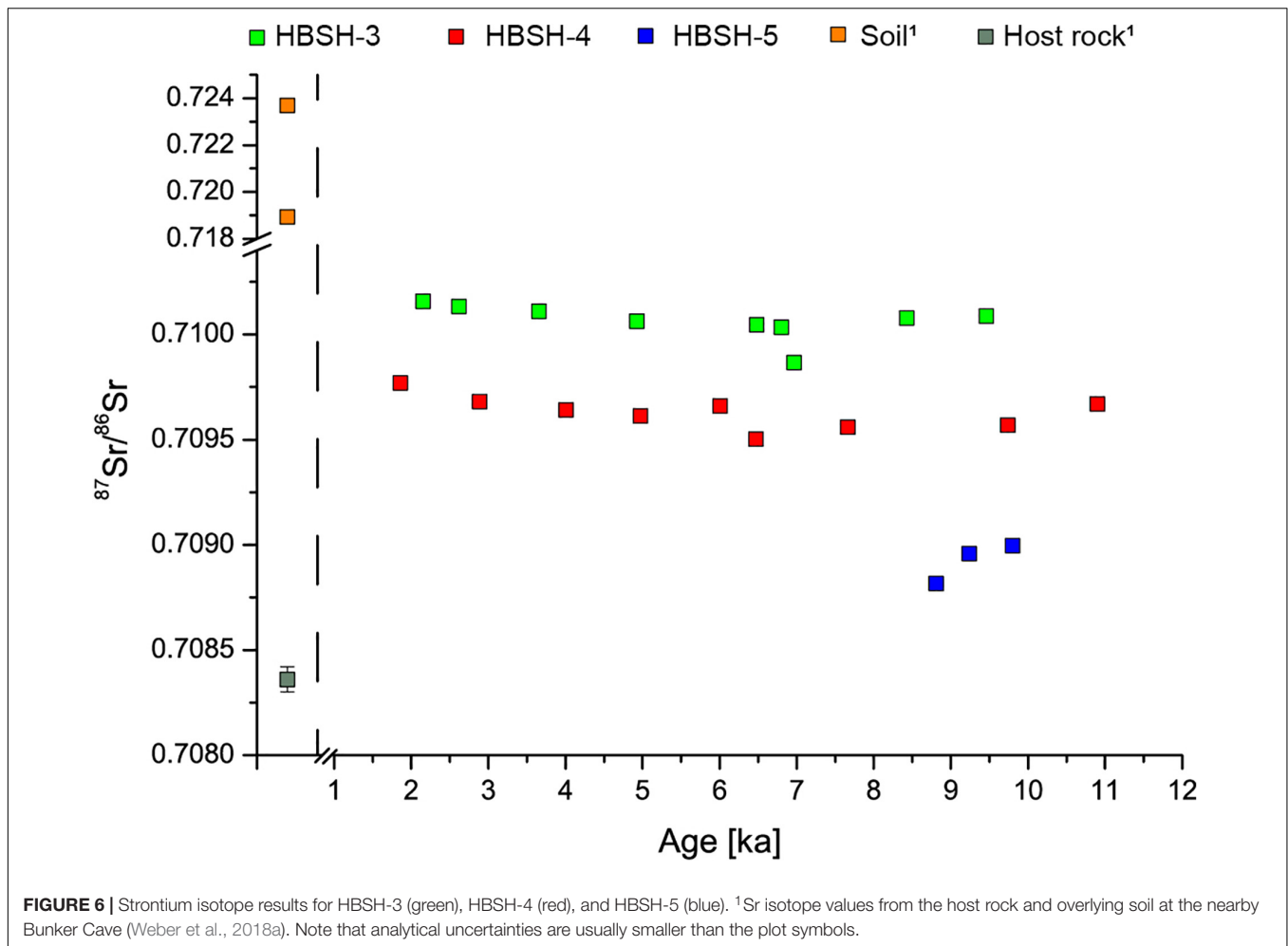
HBSH-3 has a much higher Mg concentration (1000 and 4500 μg/g). In general, Mg increases toward younger ages, especially in the second growth phase between 7.0 ± 0.2 ka and 1.3 ± 0.2 ka. Strontium and Ba show a similar trend with increasing concentrations until the growth stop and decreasing concentrations after growth resumed at 7.0 ± 0.2 ka. The opposite trend is true for P. A prominent feature is the decrease in concentration for Mg, Sr and Ba around 9.5 ± 0.2 ka.

HBSH-5 does not show large trace element variations besides an increase in Mg, Ba, and P around 8.5 ± 0.2 ka, which is contemporaneous with a decrease in Sr concentration. In general, all four observed trace element concentrations decrease toward the growth stop around 8.2 ± 0.1 ka.

Stable Isotopes

The δ¹³C values are presented in **Figure 4B**. Since the four speleothems show different growth rates, a centennial mean based on the age-depth model for each speleothem sample (**Figure 5C**) was calculated to focus on longer-term trends. Stalagmites HBSH-3 and HBSH-4 started to grow at the beginning of the Holocene, or shortly after, while growth of HBSH-5 re-initiated at that time. The three stalagmites start with similar δ¹³C values (between –8 and –9 ‰) and then rapidly tend toward more negative values until reaching their most negative values around 9.5 ka. HBSH-3 and HBSH-4 also reached their most negative δ¹³C values almost simultaneously around 9.4 ± 0.1 ka, when HBSH-5 also shows a negative peak in δ¹³C. Shortly afterward, HBSH-4 stopped growing, while HBSH-3 and HBSH-5 continued to grow until 8.3 ± 0.2 ka and 8.2 ± 0.1 ka, respectively, and show again less negative δ¹³C values. HBSH-4 started growing again around 8.2 ± 0.4 ka with δ¹³C values fluctuating between –10 and –9 ‰ with two negative peaks around 4.6 ± 0.2 ka and 3.8 (+0.6, –0.2) ka. HBSH-3 started to grow again at 7.0 ± 0.2 ka with a trend toward less negative δ¹³C values, which was further intensified after 3.0 ± 0.3 ka, reaching a peak δ¹³C value of –6.7 ‰ at 1.3 ± 0.2 ka, coherent with the final growth stop. The Holocene growth phase of the aragonitic speleothem HBSH-1 commenced at 6.1 ± 0.6 ka with an initial decrease in δ¹³C values, followed by a long-term trend toward more negative values, similar to HBSH-3. Negative δ¹³C peaks occur in HBSH-1 at 6.0 ± 0.1 ka, 4.6 ± 0.1 ka and 3.9 ± 0.1 ka, all coherent with peaks in δ¹³C values in HBSH-4. When HBSH-1 reached its most positive δ¹³C value of –6.5 ‰ at 1.3 ± 0.2 ka, HBSH-3 and HBSH-4 stopped growing, while HBSH-1 continued to grow with decreasing δ¹³C values until the final growth stop at 0.6 ± 0.1 ka.

Oxygen isotope results of all the HBSH speleothems show a general trend toward less negative δ¹⁸O values during the Holocene. As the δ¹³C values, the δ¹⁸O values (**Figure 4A**) show more variable values on annual to decadal time scales. To focus on the long-term trends, centennial means of the δ¹⁸O values (**Figure 5A**) were computed. In contrast to the δ¹³C values, the δ¹⁸O values show a more coherent trend in all speleothems. After an initial decrease shortly after growth inception in HBSH-3, HBSH-4 and HBSH-5, these three speleothems show a trend toward less negative δ¹⁸O values until their growth stops at 9.2 ± 0.4 ka (HBSH-4), 8.3 ± 0.2 ka (HBSH-3) and 8.2 ± 0.1 ka (HBSH-5). The least negative δ¹⁸O value of all speleothems is observed in HBSH-3 around 9.6 ± 0.1 ka (–4.6 ‰) and is in agreement with less negative values in HBSH-4 and HBSH-5. Subsequent to the growth stops in HBSH-3 and HBSH-4, both speleothem samples show less negative δ¹⁸O values, although HBSH-4 shows a decrease between 6.7 ± 0.3 ka and 5.8 ± 0.4 ka. Growth in the Holocene part of HBSH-1 started at 6.1 ± 0.6 ka and also tends to less negative δ¹⁸O values throughout the Holocene. The most prominent positive peak in δ¹⁸O values in HBSH-1 occurred around 5.4 ± 0.1 ka. HBSH-4 shows a coherent increase in δ¹⁸O values during that time. HBSH-1 does not show any further prominent δ¹⁸O peaks until its growth stopped around 0.6 ± 0.1 ka. However, HBSH-3 and HBSH-4 show a further trend toward



less negative $\delta^{18}\text{O}$ values around 1.7 ± 0.5 ka, which is not reflected in HBSH-1.

Strontium Isotopes

HBSH-5 shows the least radiogenic $^{87}\text{Sr}/^{86}\text{Sr}$ ratios of 0.70899 ± 0.00002 at 9.8 ± 0.2 ka and 0.70882 ± 0.00002 at 8.8 ± 0.1 ka, followed by a strongly decreasing trend toward modern time (Figure 6). HBSH-4 shows the same trend in the older growth section toward lower Sr isotope ratios. However, the $^{87}\text{Sr}/^{86}\text{Sr}$ ratios of HBSH-4 are overall higher with values between 0.70950 ± 0.00002 and 0.70977 ± 0.00002 . The lowest value of 0.70950 ± 0.00002 is observed at 6.5 ± 0.1 ka, followed by an increase toward 0.70966 ± 0.00002 at 6.0 ± 0.1 ka. Toward the final growth stop of HBSH-4 at 1.3 ± 0.2 ka, the $^{87}\text{Sr}/^{86}\text{Sr}$ ratio becomes progressively higher. HBSH-3 shows the highest Sr isotope ratios, with all $^{87}\text{Sr}/^{86}\text{Sr}$ values above 0.70987 ± 0.00002 . While the first growth phase shows identical $^{87}\text{Sr}/^{86}\text{Sr}$ within uncertainties (0.71009 ± 0.00002 and 0.71008 ± 0.00002), the second growth phase shows the lowest $^{87}\text{Sr}/^{86}\text{Sr}$ of 0.70987 ± 0.00002 at 7.0 ± 0.2 ka. Afterward, the values increase toward 0.71003 ± 0.00002 at 6.8 ± 0.2 ka and progressively become higher toward younger

ages with a maximum $^{87}\text{Sr}/^{86}\text{Sr}$ ratio of 0.71016 ± 0.00002 at 2.2 ± 0.2 ka.

DISCUSSION

Growth Phases

The four HBSH speleothem samples cover almost the entire Holocene, except the most recent 600 years. Earlier growth phases were identified between 13.6 ± 0.3 ka and 13.3 ± 0.1 ka for HBSH-4 and between 13.3 ± 0.2 ka and 12.4 ± 0.2 ka for HBSH-3 (Table 1). These initial growth phases correspond to the Bølling-Allerød interstadial (Köhler et al., 2011).

Based on the age-depth model of HBSH-4, growth during the Holocene commenced at 11.4 ± 0.1 ka. Growth of HBSH-5 re-initiated shortly afterward at 11.0 ± 0.4 ka. Based on the age model, a simultaneous growth start is possible, but this cannot be resolved. The onset of growth in HBSH-3 occurred around 10.6 ± 0.6 ka, which is shortly after HBSH-4 and HBSH-5. Therefore, it is presumed that the climate amelioration at the onset of the Holocene triggered speleothem growth in

HBSH between about 11.4 and 10.6 ka. Between 10.6 and 9.2 ka, the three speleothems grew simultaneously until HBSH-4 stopped at 9.2 ± 0.4 ka. Interestingly, when growth of HBSH-3 and HBSH-5 had stopped (8.3 ± 0.2 ka), HBSH-4 started to grow again at 8.2 ± 0.4 ka with a growth rate rapidly increasing from $<10 \mu\text{m/a}$ to up to $>100 \mu\text{m/a}$ (Figure 4G and Supplementary Figure A4). HBSH-4 growth rate declined after 6.0 ± 0.1 ka to $<10 \mu\text{m/a}$. The growth rate of HBSH-3 declined around 6.5 ± 0.4 ka with values $<10 \mu\text{m/a}$ in the same range as observed for HBSH-4 (Figure 4G and Supplementary Figure A4). Growth of HBSH-1 between 6.1 ± 0.6 ka and 0.6 ± 0.1 ka was continuous for the whole growth period, but the growth rate was very small ($< 10 \mu\text{m/a}$) and agrees with the rates observed in HBSH-3 and HBSH-4, although those are more variable (Figure 4G and Supplementary Figure A4). In general, the older growth phase during the first half of the Holocene was characterized by higher growth rates than the younger phase. The transition between these two phases in HBSH occurred between 7 and 6 ka and was marked by a reduction in growth rate. This is evident from all four speleothems from HBSH: the two speleothems covering this transition (HBSH-3 and HBSH-4) as well as the two stalagmites that only grew during one of these phases (HBSH-5 in the older phase and HBSH-1 in the younger phase).

Stable Isotopes

The $\delta^{18}\text{O}$ values of all Holocene HBSH speleothems show the same increasing trend on the long time-scale (Figures 4A, 5A). At the onset of the Holocene, $\delta^{18}\text{O}$ values are lowest in the three coeval specimens HBSH-3, HBSH-4, and HBSH-5, although their absolute values differ. A first peak in $\delta^{18}\text{O}$ values is reached around 9.4 ka, with maximum values in HBSH-3 and HBSH-4. HBSH-5 reached a stable value of ca. -5.5‰ at that time and remained at that level until the final growth stop at 8.2 ± 0.1 ka. In HBSH-3, the $\delta^{18}\text{O}$ values slightly decrease until the growth stop at 8.3 ± 0.2 ka. Simultaneously, HBSH-4 started to grow again with less negative values than prior to the growth stop and remained at that level (ca. -5‰) until 7.0 ± 0.1 ka. At that time, $\delta^{18}\text{O}$ values decrease by around 1‰ and HBSH-3 started to grow again. From that on, the $\delta^{18}\text{O}$ values increase progressively until growth finally stopped. When HBSH-1 started to grow at 6.1 ± 0.6 ka, the $\delta^{18}\text{O}$ values also progressively increased until the least negative $\delta^{18}\text{O}$ value of -4.7‰ at 0.6 ± 0.1 ka. After 5 ka, the three coeval speleothems show comparable $\delta^{18}\text{O}$ values.

For speleothem $\delta^{18}\text{O}$ values, the major influencing factors are the cave temperature and the $\delta^{18}\text{O}$ value of precipitation above the cave. The $\delta^{18}\text{O}$ value of modern precipitation in the cave region varies between -5‰ in summer and -13‰ in winter, resulting in an infiltration-weighted $\delta^{18}\text{O}$ value of -8.1‰ (Riechelmann et al., 2017). In comparison to the nearby Bunker Cave, the $\delta^{18}\text{O}$ values in the younger parts of the HBSH samples are less negative. Recent calcite precipitates from Bunker Cave show a relationship between $\delta^{18}\text{O}$ values and drip rate. The calcite $\delta^{18}\text{O}$ values for a fast-dripping site are $-6.3 \pm 0.3 \text{‰}$ and $-5.6 \pm 0.2 \text{‰}$ for a slow dripping

site (Riechelmann et al., 2013). Hence, it is reasonable to assume that the high $\delta^{18}\text{O}$ values of the HBSH stalagmites indicate very slow drip rates. However, considering that the $\delta^{18}\text{O}$ values of the HBSH stalagmites are generally higher than those of the Bunker Cave stalagmites, they were probably also influenced by additional factors. In Bunker Cave, Holocene $\delta^{18}\text{O}$ variability has been mainly attributed to changes in winter precipitation and temperature (Fohlmeister et al., 2012). In that study, less negative speleothem $\delta^{18}\text{O}$ values were interpreted to reflect cold and dry winters and vice versa. In HBSH, this interpretation would indicate a trend toward colder and dryer winters during the course of the Holocene. Besides climatic factors, disequilibrium isotope fractionation can influence the $\delta^{18}\text{O}$ values of speleothems (Lachniet, 2009; Mühlinghaus et al., 2009; Deininger et al., 2012; Hansen et al., 2019). Since a trend toward slower growth rates with time in the HBSH speleothems is observed, these disequilibrium effects may have altered the $\delta^{18}\text{O}$ values due to increasing drip intervals (Hendy, 1971; Lachniet, 2009; Riechelmann et al., 2013; Dreybrodt et al., 2016; Hansen et al., 2019), causing $\delta^{18}\text{O}$ values to increase. In addition, prior calcite precipitation (PCP) is another factor potentially influencing the stable isotope signals.

The HBSH speleothems show generally different $\delta^{13}\text{C}$ values during the first and the second part of the Holocene, starting around 7 – 6 ka (Figures 4B, 5C). After growth inception, the $\delta^{13}\text{C}$ values tend toward more negative values in HBSH-4 and HBSH-5, which is most likely related to the climate amelioration at the onset of the Holocene. Increased biological activity and vegetation development in the newly formed soil results in more negative $\delta^{13}\text{C}$ values, due to the biological fractionation of carbon in the soil with increased biological activity (McDermott, 2004). This trend is less clear for HBSH-3. However, this might be related to a later onset of growth of this speleothem, where the overlying soil and vegetation was already established. The most negative peak in $\delta^{13}\text{C}$ is reached around 9.4 ka in HBSH-3 and HBSH-4, with HBSH-5 showing a negative peak as well. This is coherent with a maximum in $\delta^{18}\text{O}$ of these three speleothems (Figures 4, 5). In general, this older phase seems to be characterized by increased soil biological activity and root respiration, indicating relatively warm and humid climate conditions during the early Holocene at HBSH. Interestingly, HBSH-4 stopped growing shortly after reaching its most negative $\delta^{13}\text{C}$ values, while HBSH-5 remains at that $\delta^{13}\text{C}$ level and HBSH-3 shows a slight trend toward less negative values until these stalagmites stopped to grow at 8.3 ± 0.2 ka and 8.2 ± 0.1 ka, respectively. At the same time, HBSH-4 resumed growth with $\delta^{13}\text{C}$ values around -10‰ and the highest growth rate of the entire stalagmite. The negative $\delta^{13}\text{C}$ values and the high growth rate suggest favorable climate conditions at that time, consistent with the Holocene climate optimum (Mayewski et al., 2004). HBSH-3 started to grow again at 7.0 ± 0.2 ka with a high growth rate and $\delta^{13}\text{C}$ values around -9.5‰ . However, growth rate in HBSH-3 rapidly declined after re-inception of growth and the $\delta^{13}\text{C}$ values increase toward -8 to -8.5‰ . This pattern is also visible in HBSH-4 around 6 ka, where the $\delta^{13}\text{C}$ values increase by more than 1‰ and

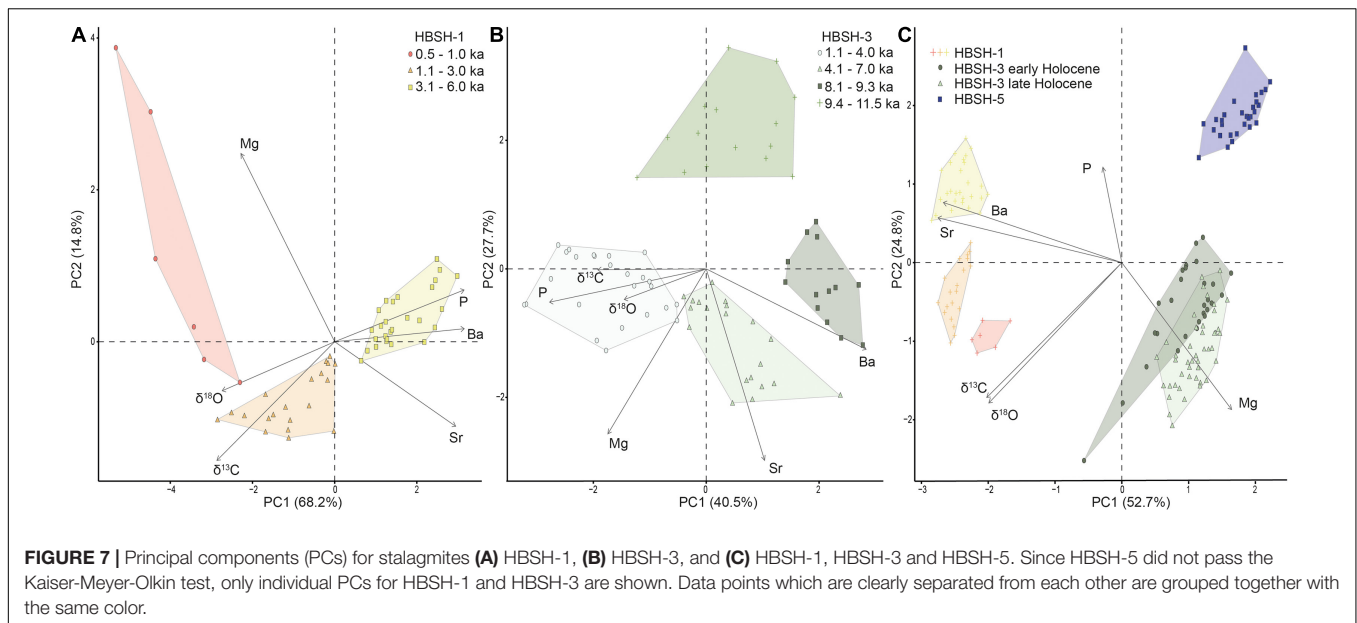
growth rate declined to less than $10 \mu\text{m/a}$. This coherent pattern indicates reduced water availability in the karst system, which can either be related to a climatic deterioration or hydrological changes in the epikarst and the vadose zone resulting in reduced water availability in the cave. Due to the observed time lag of approximately 1,000 years between the two samples, this can potentially be caused by delayed changes in the water circulation routes in the overlying karst aquifer. Shortly before the transition toward less negative $\delta^{13}\text{C}$ values and slower growth rates in HBSH-4, stalagmite HBSH-1 recommenced growing at $6.1 \pm 0.6 \text{ ka}$. The initial $\delta^{13}\text{C}$ values changed rapidly toward more negative values, before reaching a minimum at $6.0 \pm 0.1 \text{ ka}$. Further on, $\delta^{13}\text{C}$ values of HBSH-1 progressively increased. The same trend is visible in HBSH-3, while the low growth rate of HBSH-4 resulted in smoothed signals. However, some coherent patterns can be identified. At 5 ka, HBSH-1 and HBSH-4 show a simultaneous decrease in $\delta^{13}\text{C}$ until 4.5 ka, where $\delta^{13}\text{C}$ values increase in both stalagmites. A second $\delta^{13}\text{C}$ minimum is observed in all three speleothems at 4 ka. However, the general trend of $\delta^{13}\text{C}$ values is still toward higher values, reaching their maximum at $1.3 \pm 0.2 \text{ ka}$, when HBSH-3 and HBSH-4 finally stopped growing. In contrast, HBSH-1 continued to grow with a constant growth rate and decreasing $\delta^{13}\text{C}$ values (-7.8 ‰ at $0.6 \pm 0.1 \text{ ka}$).

Changes in $\delta^{13}\text{C}$ values of speleothems have often been related to environmental and climatic factors, such as vegetation cover and soil biological activity. However, due to changes in the stalagmite growth rates, (disequilibrium) isotope fractionation during speleothem deposition may introduce substantial biases. For instance, an increase in $\delta^{13}\text{C}$ values may not only reflect decreasing availability of soil CO_2 , but also a decrease in drip rate, i.e., a longer residence time of the drip water on the speleothem surface, enhancing disequilibrium isotope fractionation (Mühlinghaus et al., 2009; Scholz et al., 2009; Deininger et al., 2012; Riechelmann et al., 2013). Since growth rate remarkably dropped in all speleothems around 7 – 6 ka, it is likely that the average drip interval in HBSH increased. This is a potential cause for the progressive increase in $\delta^{13}\text{C}$ values of HBSH-1, HBSH-3, and HBSH-4 during the second half of the Holocene, because their growth rates are below $<10 \mu\text{m/a}$ during that time interval. In contrast, the first part of the Holocene was characterized by a faster growth rate and decreasing $\delta^{13}\text{C}$ values in HBSH. During this time interval, isotope disequilibrium effects on the speleothem surface played a minor role and the decreasing trend likely reflects increasing vegetation density, soil cover and biological activity.

Trace Elements

Trace elements in HBSH-5 show a decreasing trend toward the growth stop (Figure 4 and Supplementary Figure A3). At $8.5 \pm 0.2 \text{ ka}$, Mg, P, and Ba increases, while Sr decreases. This timing is coherent with the negative peaks in $\delta^{13}\text{C}$ and $\delta^{18}\text{O}$. In general, the correlation between the four investigated trace elements is positive, with Ba and P showing the highest correlation of $R = 0.70$ (Supplementary Figure A5,

$p < 4 \times 10^{-4}$). In addition, there is a positive correlation of $R = 0.49$ between $\delta^{13}\text{C}$ and Mg ($p < 7 \times 10^{-3}$), indicating PCP. Since the decrease in $\delta^{13}\text{C}$ values is attributed to soil formation and increasing biological activity, the decrease in Mg seems to be also related to these processes, i.e., enhanced soil bioproductivity and wet conditions causing lower Mg concentrations (Riechelmann et al., 2012; Wassenburg et al., 2016b; Weber et al., 2018a). Furthermore, the decrease in Mg is similar as during the initial Holocene phase in Bunker Cave (Fohlmeister et al., 2012). The authors attributed this pattern to the deposition of Mg-bearing loess during the previous glacial period and the progressive leaching of carbonate from the loess in the early Holocene. Due to the close proximity ($<1 \text{ km}$) to Bunker Cave, the same should be true for HBSH and is an additional explanation for the Mg trend observed in HBSH-5. Since HBSH-5 only covers the early part of the Holocene, the transition observed in the growth rate and stable isotopes is not captured by this speleothem. However, HBSH-3 covers most parts of the Holocene besides the hiatus between $8.3 \pm 0.2 \text{ ka}$ and $7.0 \pm 0.2 \text{ ka}$. Therefore, changes between the two different phases in HBSH-3 are expected. The first growth phase of HBSH-3 shows lower Mg concentrations than the second one. This transition is visible in the results of the PCA (Figure 7B), where Mg separates the early (11.5 – 8.1 ka) and late (7.0 – 1.1 ka) growth phases along PC2. In addition, $\delta^{13}\text{C}$ values are lower in the first growth phase. For the $\delta^{13}\text{C}$ values, the PCA especially separates the growth phases between 9.3 – 8.1 ka and 4.0 – 1.1 ka along PC1. Based on the assumption proposed for HBSH-5, the first phase is expected to have been wetter and more strongly influenced by soil formation and biological activity. Due to the increase of Mg over time, the Mg concentration is positively correlated with the $\delta^{18}\text{O}$ values ($R = 0.51$, $p < 7 \times 10^{-3}$, Supplementary Figure A6). Similar or even higher correlations exist between Mg and Sr ($R = 0.51$, $p < 6 \times 10^{-6}$) and Ba and Sr ($R = 0.78$, $p < 2 \times 10^{-14}$), indicating the same source for Ba and Sr, most likely the host rock. However, the correlation between Sr and Mg is mainly based on the first growth phase, where Ba, Sr, and Mg increase. This is clearly visible in the correlation matrix in Figure 8A, where only data from the first growth phase (10.6 ± 0.6 to $8.3 \pm 0.2 \text{ ka}$) are shown. Strontium and Ba show a strongly positive correlation ($R = 0.92$, $p < 1 \times 10^{-16}$), as well as Sr and Mg ($R = 0.72$, $p < 1 \times 10^{-16}$) and Ba and Mg ($R = 0.53$, $p < 1 \times 10^{-16}$). Magnesium, however, is slightly negatively correlated with $\delta^{13}\text{C}$ ($R = -0.19$, $p < 0.04$) and $\delta^{18}\text{O}$ ($R = -0.24$, $p < 0.005$). In the second growth phase ($7.0 \pm 0.2 \text{ ka}$ to $1.3 \pm 0.2 \text{ ka}$), Mg further increases, while Ba and Sr decrease. The correlation matrix for the younger part (Figure 8B) shows, that Mg is positively correlated with both stable isotopes during this time span ($\delta^{13}\text{C}$ $R = 0.41$, $p < 5 \times 10^{-6}$, $\delta^{18}\text{O}$ $R = 0.23$, $p < 0.02$). Furthermore, Mg is slightly negatively correlated with Ba ($R = -0.39$, $p < 3 \times 10^{-6}$), while Sr and Ba still show a strong positive correlation ($R = 0.92$, $p < 1 \times 10^{-16}$). This indicates an additional process during the younger part of the Holocene, which overprints the host rock signal for the trace elements and disrupts the relationship between Sr, Ba, and Mg, e.g., growth mechanisms of the speleothems (e.g., Paquette and Reeder, 1995;



Fairchild et al., 2000; Treble et al., 2005; Matthey et al., 2010). The increase in Mg concentration may not only be attributed to changes in pathways in the vadose zone, but also to changes in the residence time of the percolating water. PCP (Fairchild et al., 2000; Riechelmann et al., 2011) can influence the Mg concentration, with increasing PCP leading to an increase in Mg in the speleothem (Tooth and Fairchild, 2003). This could explain increasing Mg concentrations in the younger part and supports the assumption of a drier climate. In addition, differences in dissolution characteristics of calcite and dolomite (Fairchild and Treble, 2009) can cause differences in the Mg concentration. The host rock of HBSH is similar to the host rock above Bunker Cave, where dolomite is present (Grebe, 1993). During drier conditions, the contribution of dolomite to the drip water will increase and result in increased Mg concentrations in the speleothems.

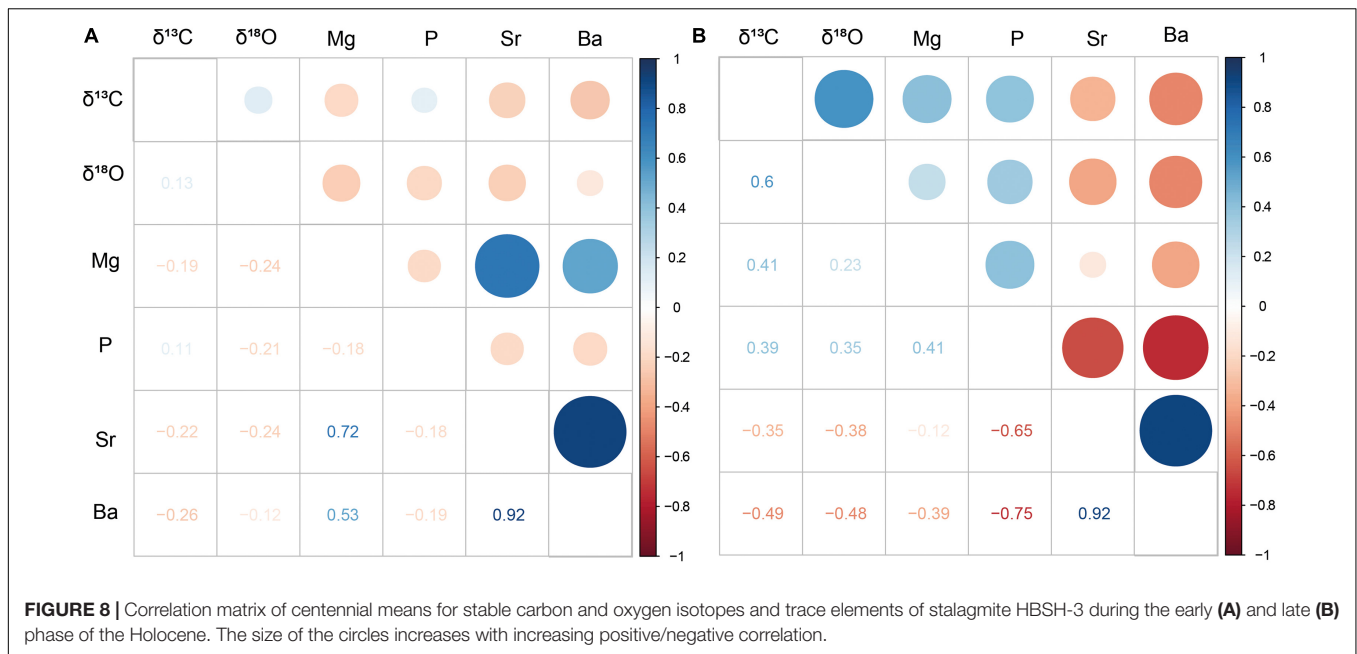
HBSH-1 shows some obvious differences in the trace element concentrations in comparison to HBSH-3 and HBSH-5 since it consists of aragonite. The Mg concentration is much lower (approximately 200 $\mu\text{g/g}$) and does not change within the stalagmite apart from some peaks in the last 1 ka. In contrast, Sr values are elevated (500 – 800 $\mu\text{g/g}$) and show minima in the youngest part, while Mg shows the opposite trend. This is related to thin layers of calcite (Jochum et al., 2012). The PCA (Figure 7A) also confirms this observation, since Mg and Sr vectors show opposite directions. This is mainly attributed to the section < 1.0 ka, where also the trace element data (Figure 4) hint toward thin layers of calcite. In general, Ba, Sr, and P show a decreasing trend toward younger ages and are positively correlated (Supplementary Figure A7). As observed in the younger part of HBSH-3, Mg is negatively correlated with Ba ($R = -0.58$, $p < 5 \times 10^{-6}$) and Sr ($R = -0.62$, $p < 5 \times 10^{-7}$). This indicates that the younger part is influenced by an additional process as described for HBSH-3. By comparing the trace element distribution between HBSH-1 and HBSH-5, which represent only

the younger and older part, respectively, the transition described for HBSH-3 is also visible. HBSH-5 shows a weak positive correlation between Mg and Ba and Sr. In contrast, the younger HBSH-1 stalagmite shows a negative correlation between Mg and Ba ($R = -0.58$, $p < 5 \times 10^{-6}$) and Sr ($R = -0.62$, $p < 5 \times 10^{-7}$).

Sr Isotopes

Strontium isotopes in speleothems have been successfully applied to assess water availability in the karst system and differences in the relative contributions of host rock and overlying soil due to changes in atmospheric deposition and weathering behavior of soils (e.g., Banner et al., 1994; Zhou et al., 2009; Belli et al., 2017; Weber et al., 2018a). Since HBSH is in close proximity to Bunker Cave and formed within the same limestone (Grebe, 1993, 1994), the host rock is expected to show the same Sr isotope signature. Therefore, the Sr isotope ratios for host rock and overlying soil reported in Weber et al. (2018a) for Bunker Cave with values of $^{87}\text{Sr}/^{86}\text{Sr} = 0.70836 \pm 0.00006$ for the host rock, 0.71893 ± 0.00001 for soil horizon C and 0.7237 ± 0.0003 for soil horizon A are used. All $^{87}\text{Sr}/^{86}\text{Sr}$ ratios of the speleothem samples lie between these end members (Figure 6), and changes in the Sr isotope composition are likely related to changes within this binary mixing system.

Similar to the changes observed for the trace elements, the Sr isotopes show a change in their trend between the early and the later growth phase. While the three studied speleothems show a trend toward less radiogenic Sr isotopes ratios in the first growth phase, shifts are observed for HBSH-3 and HBSH-4. In HBSH-3, the lowest $^{87}\text{Sr}/^{86}\text{Sr}$ is observed at 6.7 ± 0.3 ka, shortly after the onset of the second growth phase. This trend toward lower $^{87}\text{Sr}/^{86}\text{Sr}$, i.e., the value of the host rock, can be related to a longer residence time of the percolating water in the host rock after the hiatus. Therefore, the influence of the host rock Sr isotope signature increasingly affected the $^{87}\text{Sr}/^{86}\text{Sr}$ ratio of the speleothem. At 6.8 ± 0.3 ka, $^{87}\text{Sr}/^{86}\text{Sr}$ strongly increases



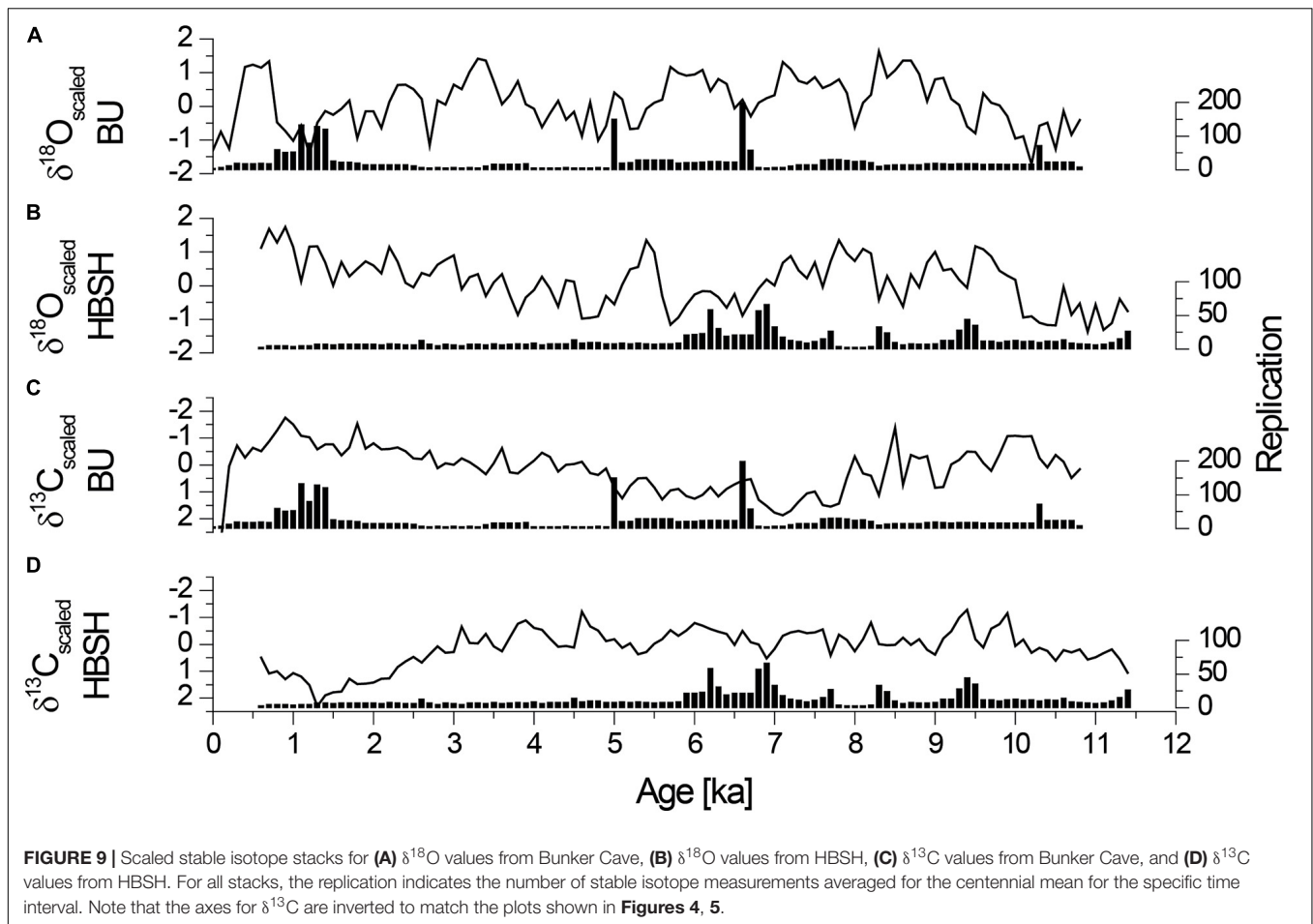
toward the growth stop. The same is true for HBSH-4, where a strong increase in $^{87}\text{Sr}/^{86}\text{Sr}$ between 6.5 and 6.0 ka is visible, coherent with a change in growth rate. Again, $^{87}\text{Sr}/^{86}\text{Sr}$ gets more radiogenic toward younger ages. The increasing $^{87}\text{Sr}/^{86}\text{Sr}$ ratios are consistent with the reduced growth rate, as well as the trend toward less negative $\delta^{13}\text{C}$ and $\delta^{18}\text{O}$ values and the increase in Mg concentration. Therefore, these factors are likely influenced by the same process, i.e., a decrease in water availability. However, this drying trend is not consistent with the Sr isotope evolution observed in Bunker Cave during the early MIS 3 (Weber et al., 2018a). In this study, two growth phases during early MIS 3 show different environmental conditions. While the early phase is believed to have been warm and humid with enhanced soil formation and a high weathering rate, the second phase was characterized by dry conditions resulting in increased $\delta^{13}\text{C}$ values and Mg concentrations. Strontium isotopes, however, tend toward less radiogenic values.

There are several different processes potentially explaining these differences. Although both cave systems lie in close proximity, the processes in the vadose zone can be highly variably and complex. In addition, environmental conditions during MIS 3 were likely different than during the Holocene. Therefore, changes in the karst system do not necessarily affect two different caves in the same way. While for Bunker Cave increased rainfall is considered to cause an overflow system in the karst reducing the influence of the host rock on the Sr isotope signature and vice versa (Riechelmann et al., 2011; Weber et al., 2018a), this is not necessarily true for HBSH. The $^{87}\text{Sr}/^{86}\text{Sr}$ ratios of the younger speleothem generation in HBSH, which suggests apparently drier conditions, may have been influenced in different ways, for instance due to changes in the relative portion of host-rock and soil-derived Sr. Thus, although the drip sites in HBSH might have been

influenced by less recharge, this may not be related to drier conditions in the catchment. In Bunker Cave, no drying trend during the Holocene was observed (Fohlmeister et al., 2012). Therefore, it is unlikely that changes in precipitation amount are responsible for the drying observed in HBSH. In contrast, changes in hydrological pathways might have caused this trend in the younger part. Consequently, the climatic conditions were still favorable and were potentially decoupled from the cave conditions.

Within-Cave Correlation of Speleothem Records From HBSH and Bunker Cave

To evaluate the significance of a single speleothem stable isotope record within HBSH, the centennial means are used to calculate correlations between the four samples, the PCA, as well as the two $\delta^{13}\text{C}$ and $\delta^{18}\text{O}$ time series (Figures 5, 7, 9, 10A). In general, the stable isotope records of the individual speleothems are highly positive correlated with the respective stack. This proves that the stack still captures the trends observed in the stalagmites. In addition, the $\delta^{18}\text{O}$ values of all four stalagmites are positively correlated with each other, suggesting a common forcing. The same is true for the $\delta^{13}\text{C}$ values. However, differences are observed when comparing the $\delta^{13}\text{C}$ and $\delta^{18}\text{O}$ values within HBSH. While the $\delta^{18}\text{O}$ record of HBSH-5 is positively correlated with the $\delta^{13}\text{C}$ records of the other speleothems, the $\delta^{13}\text{C}$ record of HBSH-5 is negatively correlated with all $\delta^{18}\text{O}$ records, as well as the $\delta^{18}\text{O}$ HBSH stack. This observation further supports the transition within the Holocene, as described in the previous sections. HBSH-5 only grew during the early phase and shows the initial decrease in $\delta^{13}\text{C}$ at the onset of the Holocene. Thus, this specimen does not record the transition. The $\delta^{13}\text{C}$ and $\delta^{18}\text{O}$ stacks are weakly positively correlated ($R = 0.33$, $p < 5 \times 10^{-4}$). However, this correlation is mainly caused



by the same trend in the youngest section, which is strongly expressed by the positive correlation between the $\delta^{13}\text{C}$ stack and the $\delta^{18}\text{O}$ record of HBSH-1 ($R = 0.65$, $p < 8 \times 10^{-8}$) and the $\delta^{18}\text{O}$ stack and the $\delta^{13}\text{C}$ record of HBSH-1 ($R = 0.69$, $p < 4 \times 10^{-9}$).

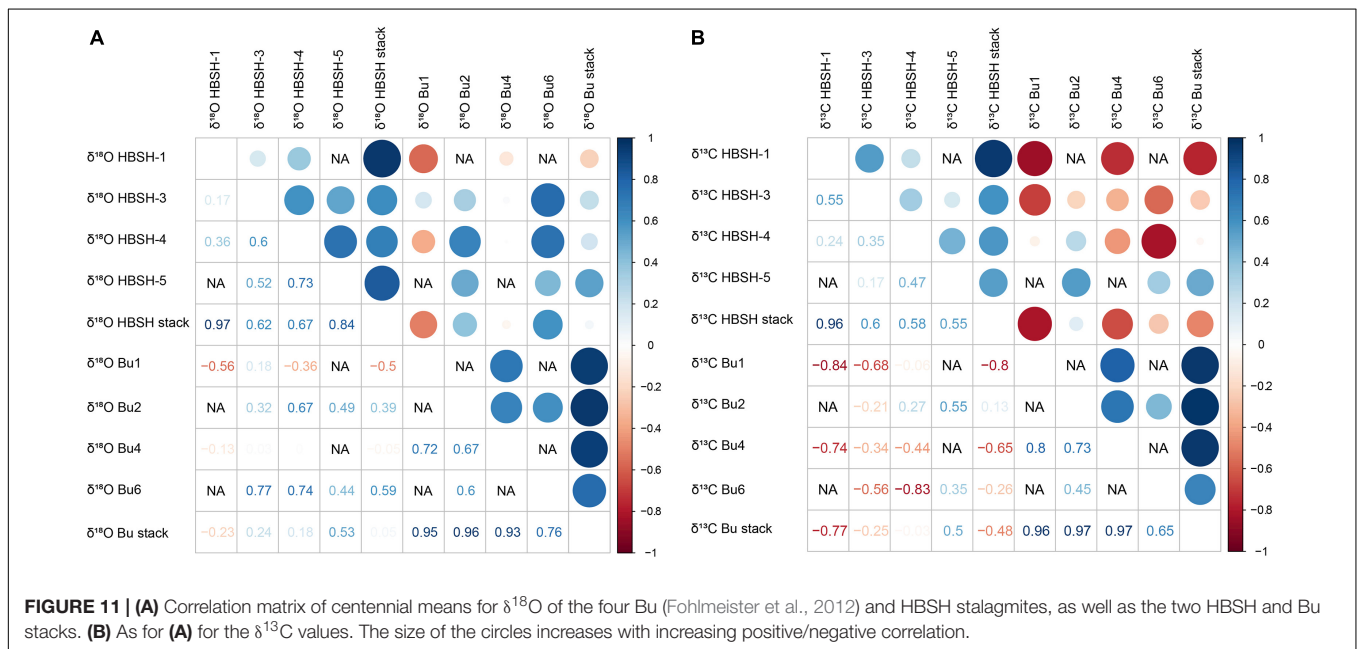
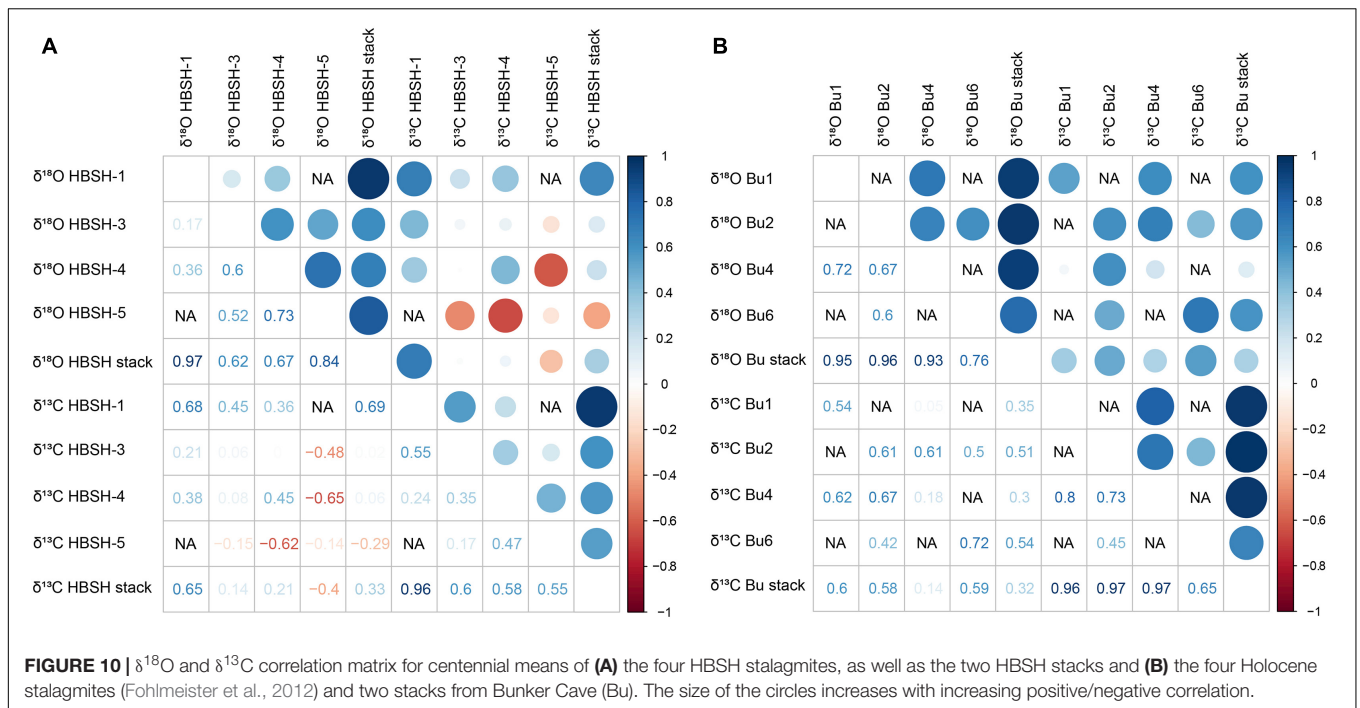
The PCA including HBSH-1, HBSH-3, and HBSH-5 (Figure 7C) shows a clear separation between the three stalagmites, without any overlap. In addition, a further separation within HBSH-1 and in HBSH-3 is visible. In principle, both stable isotope values separate HBSH-1 and HBSH-5 from each other and show a strong anti-correlation. While HBSH-5 groups together, HBSH-1 is separated in three different clusters (Figures 7A,C). HBSH-3 is the only stalagmite in the PCA which covers almost the whole Holocene and where differences between the early and late growth phase (Figure 8) are expected. The PCA confirms that Mg, Sr and Ba are the main separators for this sample and that $\delta^{13}\text{C}$ and $\delta^{18}\text{O}$ start to diverge during the late Holocene (Figure 7B). The overall separation between the three stalagmites shows that each is dependent of other processes, i.e., the difference between aragonite and calcite, as well as the time of formation.

In contrast to HBSH, the correlation matrix for Bunker Cave (Figure 10B) shows positive correlations between all

stalagmites and isotope curves, covering the same time interval. This indicates that these two isotope systems were influenced by similar processes, as all individual samples show a positive correlation with the $\delta^{13}\text{C}$ and $\delta^{18}\text{O}$ stacks, for the same as well as for the other isotope.

Inter-Cave Correlation of Speleothem Records From HBSH and Bunker Cave

The two $\delta^{18}\text{O}$ stacks for HBSH and Bunker Cave are not significantly correlated (Figures 9, 11A). This is largely related to differences in the correlations of individual speleothems. While Bu2 and Bu6 show positive but insignificant correlations with all HBSH stalagmites covering the same time span, Bu4 does not show any correlation with HBSH specimens. Bu1 even shows negative correlations with the HBSH $\delta^{18}\text{O}$ records. This indicates, that the Bu speleothems do not show an overall common $\delta^{18}\text{O}$ trend as described for HBSH. However, the Bunker Cave speleothems do not overlap as much as the HBSH speleothems in their growth history. Thus, the resulting Bunker Cave stack is largely influenced by stalagmite Bu4, which grew from 8 ka until recent times. Since Bu4 does not show any correlation with the HBSH speleothems, the lack of correlation between the HBSH and the Bunker Cave stacks is reasonable. These



findings further support the strong transition in the HBSH records during the middle Holocene. The positive correlation of Bu2 and Bu6 during the early Holocene shows that during that time the records from both caves capture a common signal. However, since Bu4 and Bu1 started to grow around 8 and 6 ka, respectively, both stalagmites mainly cover periods when HBSH is expected to be already influenced by cave-specific processes.

For the $\delta^{13}\text{C}$ records (Figure 11B), the comparison between the two cave systems yielded significantly negative correlations.

This is especially true for HBSH-1 and the coeval stalagmites Bu1 ($R = -0.56, p < 2 \times 10^{-7}$) and Bu4 ($R = -0.74, p < 2 \times 10^{-10}$), which grew during the late Holocene. In addition, HBSH-3 shows negative correlations with all Bunker Cave stalagmites, although covering large parts of the Holocene. A different pattern is visible for HBSH-4, which indicates a weak positive correlation with Bu2, which grew during the early Holocene until approximately 8 ka. In contrast, the comparison with Bu4 yielded a negative correlation ($R = -0.44, p < 3 \times 10^{-4}$). Interestingly, the $\delta^{13}\text{C}$ values of HBSH-5 show a positive correlation with the coeval Bu2

($R = 0.55, p < 3 \times 10^{-3}$) stalagmite, which grew during the early Holocene. This indicates, that the early Holocene $\delta^{13}\text{C}$ signal is consistently registered in both HBSH and Bunker Cave, while later on, the $\delta^{13}\text{C}$ trends become dispersed and yield negative correlations. This observation is in agreement with the previously observed transition in the stable isotope, trace element and Sr isotope records.

The comparison of the stable isotope stacks from the two caves (Figure 9) underscores the results of the correlation analysis. For the $\delta^{18}\text{O}$ values, the first part of the Holocene shows some common features between HBSH and Bunker Cave speleothems, such as a peak around 9.6 ka and a general trend toward less negative values. However, this pattern disappears or even reverses in the late Holocene, especially for the youngest 3 – 4 ka, where the trends are opposite. Similar patterns can be observed in the $\delta^{13}\text{C}$ stack, with a trend toward more negative $\delta^{13}\text{C}$ values in the first part until ca. 9.5 ka, recorded in both caves. This represents the onset of the Holocene with increased vegetation and soil formation. However, from 7 – 6 ka onward, a pronounced trend of divergence is observed. At 6.5 ka, the $\delta^{13}\text{C}$ values in Bunker Cave become progressively more negative, while the $\delta^{13}\text{C}$ values in HBSH tend toward less negative values after 6 ka, resulting in a strongly negative correlation.

Implications for Speleothem-Based Palaeoclimate Reconstructions

Our results show that the use of stable isotopes for palaeoclimate reconstructions using speleothems may be strongly biased by non-climatic/non-environmental factors. Although HBSH and Bunker Cave are less than 1 km apart, the stable isotope records of stalagmites from these caves lack a consistent pattern for large parts of the Holocene. The speleothems from HBSH show a trend toward less negative $\delta^{13}\text{C}$ values during the last 6 ka. This could be interpreted as a general trend toward drier conditions, less vegetation cover and reduced soil biological activity, associated with a less humid climate. However, by comparing these results with the much more intensively studied Bunker Cave dataset (including both cave monitoring and palaeoclimate studies, e.g., Riechelmann et al., 2011, 2017; Fohlmeister et al., 2012; Weber et al., 2018a) and other well-established climate archives for the same time interval (e.g., Wanner et al., 2008; Fohlmeister et al., 2013; Sirocko et al., 2016), this interpretation is unlikely. Growth rate and the trace element composition of the speleothems suggest that the increase in the $\delta^{13}\text{C}$ values, and probably also the $\delta^{18}\text{O}$ values, mainly results from disequilibrium isotope fractionation on the speleothem surface due to increased drip intervals and/or PCP. Besides these general differences between the two cave systems, there are also differences between individual speleothem records from the same cave. While the aragonitic HBSH-1 stalagmite shows a strong positive correlation between the two isotopes, the calcitic HBSH-5 stalagmite yields a slightly negative correlation. Not all speleothems from the same cave grew simultaneously. Monitoring studies of cave systems have shown that not necessarily all drip sites within a cave yielded a geochemically consistent picture. For instance, Musgrove and

Banner (2004) showed that the hydro-geochemistry ($^{87}\text{Sr}/^{86}\text{Sr}$, Sr/Ca, and Mg/Ca) of different drip sites in a cave in central Texas is temporally and spatially variable. Other studies showed that also the drip rate of drip sites within the same cave (Ciur-Izbuca Cave, Romania) can be significantly different and decoupled from rainfall (Moldovan et al., 2018). This is further supported by a study identified a chaotic discharge behavior in Cathedral Cave (Australia), which especially influences growth-rate dependent climate proxies (Mariethoz et al., 2012). This highlights the complex interplay between processes in the karst system and the growth dynamics of speleothems. Therefore, reconstructions based on single speleothems should be viewed with caution and replication, as well as a multi-proxy approach together with statistical approaches should be applied to disentangle potential site-specific cave effects from environmental signals.

CONCLUSION

By comparing stable isotope records from HBSH and the nearby Bunker Cave, both differences between the two caves and within the individual stalagmites from HBSH were identified. While the proxy records show similar trends in both caves for the early Holocene, a diverging pattern, especially in the $\delta^{13}\text{C}$ values was observed during the late Holocene. By using a multi-proxy approach of stable isotopes, trace elements and Sr isotopes, it is possible to show that the younger part in HBSH was largely influenced by a drying of the karst system, causing an increase in $\delta^{13}\text{C}$ and $\delta^{18}\text{O}$ values due to disequilibrium fractionation and PCP. This shows that individual stalagmites may faithfully capture climatic and environmental signals, while stalagmites from other parts of the same cave may be strongly influenced by highly localized cave-internal processes. Replicating stalagmite records and applying several proxies is therefore essential to obtain robust palaeoclimate information.

DATA AVAILABILITY STATEMENT

The original contributions presented in the study are included in the article and **Supplementary Material**, further inquiries can be directed to the corresponding author.

AUTHOR CONTRIBUTIONS

MW, DS, and YH designed the study. MW, YH, DS, BS, and CS performed the stable isotope analysis and interpretation. MW, YH, DS, DH, and KJ was performed dating of the samples. YH, KJ, and DS performed Trace element analysis and data evaluation. MW performed Strontium isotope analysis and the regression analysis, and wrote the manuscript, DS, BS, CS, DR, and KJ improved the manuscript. All authors discussed the results and commented on the manuscript.

FUNDING

MW, KJ, and DS are grateful to the Max Planck Graduate Center and the German Research Foundation (DFG SCHO 1274/9-1 and SCHO 1274/11-1) for funding.

ACKNOWLEDGMENTS

We thank B. Schwager, B. Stoll, U. Weis, M. Wimmer, M. Maus, and M. Großkopf for assistance in the laboratory and K.

Weber for discussion of the PCA. Detailed and constructive comments and suggestions of two reviewers and the editor are greatly acknowledged.

SUPPLEMENTARY MATERIAL

The Supplementary Material for this article can be found online at: <https://www.frontiersin.org/articles/10.3389/feart.2021.642651/full#supplementary-material>

REFERENCES

- Bajo, P., Hellstrom, J., Frisia, S., Drysdale, R., Black, J., Woodhead, J., et al. (2016). "Cryptic" diagenesis and its implications for speleothem geochronologies. *Quat. Sci. Rev.* 148, 17–28. doi: 10.1016/j.quascirev.2016.06.020
- Banner, J. L., Musgrove, M., and Capo, R. C. (1994). Tracing ground-water evolution in a limestone aquifer using Sr isotopes: effects of multiple sources of dissolved ions and mineral-solution reactions. *Geology* 22, 687–690. doi: 10.1130/0091-7613(1994)022<0687:TGWIEA>2.3.CO;2
- Banner, J. L., Musgrove, M. L., Asmerom, Y., Edwards, R. L., and Hoff, J. A. (1996). High-resolution temporal record of holocene ground-water chemistry: tracing links between climate and hydrology. *Geology* 24, 1049–1053. doi: 10.1130/0091-7613(1996)024<1049:HRTROH>2.3.CO;2
- Bartlett, M. S. (1937). Properties of sufficiency and statistical tests. *Proc. R. Soc. Lond. Ser. A Math. Phys. Sci.* 160, 268–282. doi: 10.1098/rspa.1937.0109
- Belli, R., Borsato, A., Frisia, S., Drysdale, R., Maas, R., and Greig, A. (2017). Investigating the hydrological significance of stalagmite geochemistry (Mg, Sr) using Sr isotope and particulate element records across the Late Glacial-to-Holocene transition. *Geochim. Cosmochim. Acta* 199, 247–263. doi: 10.1016/j.gca.2016.10.024
- Breitenbach, S. F. M., Rehfeld, K., Goswami, B., Baldini, J. U. L., Ridley, H. E., Kennett, D., et al. (2012). CO2 reconstruction from ice cores (COPRA). *Clim. Past* 8, 1765–1779. doi: 10.5194/cp-8-1765-2012
- Budaev, S. V. (2010). Using principal components and factor analysis in animal behaviour research: caveats and guidelines. *Ethology* 116, 472–480. doi: 10.1111/j.1439-0310.2010.01758.x
- Budsky, A., Scholz, D., Wassenburg, J. A., Mertz-Kraus, R., Spötl, C., Riechelmann, D. F. C., et al. (2019). Speleothem $\delta^{13}\text{C}$ record suggests enhanced spring/summer drought in south-eastern Spain between 9.7 and 7.8 ka—A circum-Western Mediterranean anomaly? *Holocene* 29, 1113–1133. doi: 10.1177/0959683619838021
- Burchette, T. P. (1981). European devonian reefs: a review of current concepts and models. *SEPM Special Publ.* 30, 85–142. doi: 10.2110/pec.81.30.0085
- Cheng, H., Edwards, R. L., Hoff, J., Gallup, C. D., Richards, D. A., and Asmerom, Y. (2000). The half-lives of uranium-234 and thorium-230. *Chem. Geol.* 169, 17–33. doi: 10.1016/S0009-2541(99)00157-6
- Cheng, H., Lawrence Edwards, R., Shen, C.-C., Polyak, V. J., Asmerom, Y., Woodhead, J., et al. (2013). Improvements in ^{230}Th dating, ^{230}Th and ^{234}U half-life values, and U–Th isotopic measurements by multi-collector inductively coupled plasma mass spectrometry. *Earth Planet. Sci. Lett.* 371–372, 82–91. doi: 10.1016/j.epsl.2013.04.006
- Comas-Bru, L., Rehfeld, K., Roesch, C., Amirnezhad-Mozhdehi, S., Harrison, S. P., Atsawaranant, K., et al. (2020). SISALv2: a comprehensive speleothem isotope database with multiple age–depth models. *Earth Syst. Sci. Data* 12, 2579–2606. doi: 10.5194/essd-12-2579-2020
- Deininger, M., Fohlmeister, J., Scholz, D., and Mangini, A. (2012). Isotope disequilibrium effects: the influence of evaporation and ventilation effects on the carbon and oxygen isotope composition of speleothems – A model approach. *Geochim. Cosmochim. Acta* 96, 57–79. doi: 10.1016/j.gca.2012.08.013
- Dettman, D. L., and Lohmann, K. C. (1995). Microsampling carbonates for stable isotope and minor element analysis; physical separation of samples on a 20 micrometer scale. *J. Sediment. Res.* 65, 566–569. doi: 10.1306/D426813F-2B26-11D7-8648000102C1865D
- Dreybrodt, W., Hansen, M., and Scholz, D. (2016). Processes affecting the stable isotope composition of calcite during precipitation on the surface of stalagmites: laboratory experiments investigating the isotope exchange between DIC in the solution layer on top of a speleothem and the CO_2 of the cave atmosphere. *Geochim. Cosmochim. Acta* 174, 247–262. doi: 10.1016/j.gca.2015.11.012
- Fairchild, I. J., Borsato, A., Tooth, A. F., Frisia, S., Hawkesworth, C. J., Huang, Y., et al. (2000). Controls on trace element (Sr–Mg) compositions of carbonate cave waters: implications for speleothem climatic records. *Chem. Geol.* 166, 255–269. doi: 10.1016/S0009-2541(99)00216-8
- Fairchild, I. J., Smith, C. L., Baker, A., Fuller, L., Spotl, C., Matthey, D., et al. (2006). Modification and preservation of environmental signals in speleothems. *Earth Sci. Rev.* 75, 105–153. doi: 10.1016/j.earscirev.2005.08.003
- Fairchild, I. J., and Treble, P. C. (2009). Trace elements in speleothems as recorders of environmental change. *Quat. Sci. Rev.* 28, 449–468. doi: 10.1016/j.quascirev.2008.11.007
- Fankhauser, A., Mcdermott, F., and Fleitmann, D. (2016). Episodic speleothem deposition tracks the terrestrial impact of millennial-scale last glacial climate variability in SW Ireland. *Quat. Sci. Rev.* 152, 104–117. doi: 10.1016/j.quascirev.2016.09.019
- Fohlmeister, J., Schröder-Ritzrau, A., Scholz, D., Spötl, C., Riechelmann, D. F. C., Mudelsee, M., et al. (2012). Bunker Cave stalagmites: an archive for central European Holocene climate variability. *Clim. Past* 8, 1751–1764. doi: 10.5194/cp-8-1751-2012
- Fohlmeister, J., Vollweiler, N., Spötl, C., and Mangini, A. (2013). COMNISPA II: update of a mid-European isotope climate record, 11 ka to present. *Holocene* 23, 749–754. doi: 10.1177/0959683612465446
- Genty, D., Blamart, D., Ouahdi, R., Gilmour, M., Baker, A., Jozel, J., et al. (2003). Precise dating of dansgaard-oeschger climate oscillations in western Europe from stalagmite data. *Nature* 421, 833–837. doi: 10.1038/nature01391
- Gibert, L., Scott, G. R., Scholz, D., Budsky, A., Ferrández, C., Ribot, F., et al. (2016). Chronology of the Cueva Victoria fossil site (SE Spain): evidence for Early Pleistocene Afro-Iberian dispersals. *J. Hum. Evol.* 90, 183–197. doi: 10.1016/j.jhevol.2015.08.002
- Grebe, W. (1993). Die bunkerhöhle in iserlohn-letmathe (Sauerland). *Mitteilung des Verbands der deutschen Höhlen-und Karstforscher, München* 39, 22–23.
- Grebe, W. (1994). Die Hüttenbläseerschachthöhle—eine neu entdeckte Höhle in Iserlohn-Letmathe. *Mitteilungen & Berichte Speläogruppe Letmathe* 10, 49–65.
- Hammerschmidt, E., Niggemann, S., Grebe, W., Oelze, R., Brix, M. R., and Richter, D. K. (1995). Höhlen in Iserlohn.—Schriften zur Karst- und Höhlenkunde in Westfalen Heft 1, Iserlohn, 154.
- Hansen, M., Scholz, D., Froeschmann, M.-L., Schöne, B. R., and Spötl, C. (2017). Carbon isotope exchange between gaseous CO_2 and thin solution films: artificial cave experiments and a complete diffusion-reaction model. *Geochim. Cosmochim. Acta* 211, 28–47. doi: 10.1016/j.gca.2017.05.005
- Hansen, M., Scholz, D., Schöne, B. R., and Spötl, C. (2019). Simulating speleothem growth in the laboratory: determination of the stable isotope fractionation ($\delta^{13}\text{C}$ and $\delta^{18}\text{O}$) between H_2O , DIC and CaCO_3 . *Chem. Geol.* 509, 22–44. doi: 10.1016/j.chemgeo.2018.12.012
- Hendy, C. H. (1971). The isotopic geochemistry of speleothems—I. The calculation of the effects of different modes of formation on the isotopic composition

- of speleothems and their applicability as palaeoclimatic indicators. *Geochim. Cosmochim. Acta* 35, 801–824. doi: 10.1016/0016-7037(71)90127-X
- Hoffmann, D. L. (2008). 230Th isotope measurements of femtogram quantities for U-series dating using multi ion counting (MIC) MC-ICPMS. *Int. J. Mass Spectrom.* 275, 75–79. doi: 10.1016/j.ijms.2008.05.033
- Hoffmann, D. L., Prytulak, J., Richards, D. A., Elliott, T., Coath, C. D., Smart, P. L., et al. (2007). Procedures for accurate U and Th isotope measurements by high precision MC-ICPMS. *Int. J. Mass Spectrom.* 264, 97–109. doi: 10.1016/j.ijms.2007.03.020
- Hori, M., Ishikawa, T., Nagaishi, K., Lin, K., Wang, B.-S., You, C.-F., et al. (2013). Prior calcite precipitation and source mixing process influence Sr/Ca, Ba/Ca and ⁸⁷Sr/⁸⁶Sr of a stalagmite developed in southwestern Japan during 18.0–4.5 ka. *Chem. Geol.* 347, 190–198. doi: 10.1016/j.chemgeo.2013.03.005
- Jochum, K. P., Scholz, D., Stoll, B., Weis, U., Wilson, S. A., Yang, Q. C., et al. (2012). Accurate trace element analysis of speleothems and biogenic calcium carbonates by LA-ICP-MS. *Chem. Geol.* 318, 31–44. doi: 10.1016/j.chemgeo.2012.05.009
- Kaiser, H. F. (1970). A second generation little jiffy. *Psychometrika* 35, 401–415. doi: 10.1007/BF02291817
- Kaiser, H. F., and Rice, J. (1974). Little jiffy, mark IV. *Educ. Psychol. Meas.* 34, 111–117. doi: 10.1177/001316447403400115
- Köhler, P., Knorr, G., Buiron, D., Lourantou, A., and Chappellaz, J. (2011). Abrupt rise in atmospheric CO₂ at the onset of the Bølling/Allerød: in-situ ice core data versus true atmospheric signal. *Clim. Past* 7, 473–486. doi: 10.5194/cp-7-473-2011
- Krebs, W. (1974). Devonian carbonate complexes of Central Europe. *Soc. Econ. Paleontol. Mineral. Special Publ.* 18, 155–208. doi: 10.2110/pec.74.18.0155
- Lachniet, M. S. (2009). Climatic and environmental controls on speleothem oxygen-isotope values. *Quat. Sci. Rev.* 28, 412–432. doi: 10.1016/j.quascirev.2008.10.021
- Lechleitner, F. A., Amirnezhad-Mozhdehi, S., Columbu, A., Comas-Bru, L., Labuhn, I., Pérez-Mejías, C., et al. (2018). The potential of speleothems from Western Europe as recorders of regional climate: a critical assessment of the SISAL database. *Quaternary* 1:30. doi: 10.3390/quat1030030
- Li, H.-C., Ku, T.-L., You, C.-F., Cheng, H., Edwards, R. L., Ma, Z.-B., et al. (2005). ⁸⁷Sr/⁸⁶Sr and Sr/Ca in speleothems for paleoclimate reconstruction in Central China between 70 and 280 kyr ago. *Geochim. Cosmochim. Acta* 69, 3933–3947. doi: 10.1016/j.gca.2005.01.009
- Lin, Y., Jochum, K. P., Scholz, D., Hoffmann, D. L., Stoll, B., Weis, U., et al. (2017). In-situ high spatial resolution LA-MC-ICPMS 230Th/U dating enables detection of small-scale age inversions in speleothems. *Solid Earth Sci.* 2, 1–9. doi: 10.1016/j.sesci.2016.12.003
- Luetscher, M., Boch, R., Sodemann, H., Spötl, C., Cheng, H., Edwards, R. L., et al. (2015). North Atlantic storm track changes during the Last Glacial Maximum recorded by Alpine speleothems. *Nat. Commun.* 6:6344. doi: 10.1038/ncomms7344
- Lugli, F., Cipriani, A., Peretto, C., Mazzucchelli, M., and Brunelli, D. (2017). In situ high spatial resolution ⁸⁷Sr/⁸⁶Sr ratio determination of two Middle Pleistocene (c.a. 580 ka) Stephanorhinus hundsheimensis teeth by LA-MC-ICP-MS. *Int. J. Mass Spectrom.* 412, 38–48. doi: 10.1016/j.ijms.2016.12.012
- Mangini, A., Verdes, P., Spötl, C., Scholz, D., Vollweiler, N., and Kromer, B. (2007). Persistent influence of the North Atlantic hydrography on central European winter temperature during the last 9000 years. *Geophys. Res. Lett.* 34:L02704. doi: 10.1029/2006GL028600
- Mariethoz, G., Baker, A., Sivakumar, B., Hartland, A., and Graham, P. (2012). Chaos and irregularity in karst percolation. *Geophys. Res. Lett.* 39:L23305. doi: 10.1029/2012GL054270
- Matthey, D. P., Fairchild, I. J., Atkinson, T. C., Latin, J.-P., Ainsworth, M., and Durell, R. (2010). Seasonal microclimate control of calcite fabrics, stable isotopes and trace elements in modern speleothem from St Michaels Cave, Gibraltar. *Geol. Soc. Lond. Special Publ.* 336, 323–344. doi: 10.1144/SP336.17
- Mayewski, P. A., Rohling, E. E., Curt Stager, J., Karlén, W., Maasch, K. A., David Meeker, L., et al. (2004). Holocene climate variability. *Quat. Res.* 62, 243–255. doi: 10.1016/j.yqres.2004.07.001
- McArthur, J. M., Howarth, R. J., and Bailey, T. R. (2001). Strontium isotope stratigraphy: LOWESS Version 3: best fit to the marine Sr-Isotope Curve for 0–509 Ma and accompanying look-up table for deriving numerical age. *J. Geol.* 109, 155–170. doi: 10.1086/319243
- McDermott, F. (2004). Palaeo-climate reconstruction from stable isotope variations in speleothems: a review. *Quat. Sci. Rev.* 23, 901–918. doi: 10.1016/j.quascirev.2003.06.021
- McDermott, F., Frisia, S., Huang, Y., Longinelli, A., Spiro, B., Heaton, T. H. E., et al. (1999). Holocene climate variability in Europe: evidence from δ¹⁸O, textural and extension-rate variations in three speleothems. *Quat. Sci. Rev.* 18, 1021–1038. doi: 10.1016/S0277-3791(98)00107-3
- Mickler, P. J., Stern, L. A., and Banner, J. L. (2006). Large kinetic isotope effects in modern speleothems. *Geol. Soc. Am. Bull.* 118, 65–81. doi: 10.1130/B25698.1
- Mischel, S. A., Scholz, D., Spötl, C., Jochum, K. P., Schröder-Ritzrau, A., and Fiedler, S. (2017a). Holocene climate variability in Central Germany and a potential link to the polar North Atlantic: a replicated record from three coeval speleothems. *Holocene* 27, 509–525. doi: 10.1177/0959683616670246
- Mischel, S. A., Mertz-Kraus, R., Jochum Klaus, P., and Scholz, D. (2017b). TERMITE: an R script for fast reduction of laser ablation inductively coupled plasma mass spectrometry data and its application to trace element measurements. *Rapid Commun. Mass Spectrom.* 31, 1079–1087. doi: 10.1002/rcm.7895
- Moldovan, O. T., Constantin, S., and Cheval, S. (2018). Drip heterogeneity and the impact of decreased flow rates on the vadose zone fauna in Ciur-Izbuca Cave, NW Romania. *Ecohydrology* 11:e2028. doi: 10.1002/eco.2028
- Moseley, G. E., Spötl, C., Svensson, A., Cheng, H., Brandstätter, S., and Edwards, R. L. (2014). Multi-speleothem record reveals tightly coupled climate between central Europe and Greenland during Marine Isotope Stage 3. *Geology* 42, 1043–1046. doi: 10.1130/G36063.1
- Mühlhlinghaus, C., Scholz, D., and Mangini, A. (2009). Modelling fractionation of stable isotopes in stalagmites. *Geochim. Cosmochim. Acta* 73, 7275–7289. doi: 10.1016/j.gca.2009.09.010
- Musgrove, M., and Banner, J. L. (2004). Controls on the spatial and temporal variability of vadose dripwater geochemistry: edwards aquifer, central Texas. *Geochim. Cosmochim. Acta* 68, 1007–1020. doi: 10.1016/j.gca.2003.08.014
- Niggemann, S., Mangini, A., Richter, D. K., and Wurth, G. (2003). A paleoclimate record of the last 17,600 years in stalagmites from the B7 cave, Sauerland, Germany. *Quat. Sci. Rev.* 22, 555–567. doi: 10.1016/S0277-3791(02)00143-9
- Obert, J. C., Scholz, D., Felis, T., Brocas, W. M., Jochum, K. P., and Andreae, M. O. (2016). ²³⁰Th/U dating of last interglacial brain corals from bonaire (southern Caribbean) using bulk and theca wall material. *Geochim. Cosmochim. Acta* 178, 20–40. doi: 10.1016/j.gca.2016.01.011
- Paeckelmann, W. (1922). Der mitteldevonische massenkalk des bergischen landes. *Abhandlungen der Preußischen Geologischen Landesanstalt* 91, 1–112. doi: 10.5962/bhl.title.134334
- Paquette, J., and Reeder, R. J. (1995). Relationship between surface structure, growth mechanism, and trace element incorporation in calcite. *Geochim. Cosmochim. Acta* 59, 735–749. doi: 10.1016/0016-7037(95)00004-J
- R Core Team (2020). *R: A Language and Environment for Statistical Computing*. Vienna: R Core Team.
- Richter, D. K., Goll, K., Grebe, W., Niedermayr, A., Platte, A., and Scholz, D. (2015). Weichselzeitliche Kryocalcite als Hinweise für Eisseen in der Hüttenblärschachthöhle (Iserlohn/NRW). *Quat. Sci. J.* 64, 67–81. doi: 10.3285/eg.64.2.02
- Riechelmann, D. F. C., Deininger, M., Scholz, D., Riechelmann, S., Schröder-Ritzrau, A., Spötl, C., et al. (2013). Disequilibrium carbon and oxygen isotope fractionation in recent cave calcite: comparison of cave precipitates and model data. *Geochim. Cosmochim. Acta* 103, 232–244. doi: 10.1016/j.gca.2012.11.002
- Riechelmann, D. F. C., Schröder-Ritzrau, A., Scholz, D., Fohlmeister, J., Spötl, C., Richter, D. K., et al. (2011). Monitoring bunker cave (NW Germany): a prerequisite to interpret geochemical proxy data of speleothems from this site. *J. Hydrol.* 409, 682–695. doi: 10.1016/j.jhydrol.2011.08.068
- Riechelmann, S., Buhl, D., Schröder-Ritzrau, A., Riechelmann, D. F. C., Richter, D. K., Vohnhof, H. B., et al. (2012). The magnesium isotope record of cave carbonate archives. *Clim. Past* 8, 1849–1867. doi: 10.5194/cp-8-1849-2012
- Riechelmann, S., Schröder-Ritzrau, A., Spötl, C., Riechelmann, D. F. C., Richter, D. K., Mangini, A., et al. (2017). Sensitivity of Bunker Cave to climatic forcings highlighted through multi-annual monitoring of rain-, soil-, and dripwaters. *Chem. Geol.* 449, 194–205. doi: 10.1016/j.chemgeo.2016.12.015

- Scholz, D., and Hoffmann, D. (2008). $^{230}\text{Th}/\text{U}$ -dating of fossil corals and speleothems. *Quat. Sci. J.* 57, 52–76. doi: 10.3285/eg.57.1-2.3
- Scholz, D., and Hoffmann, D. L. (2011). StalAge-An algorithm designed for construction of speleothem age models. *Quat. Geochronol.* 6, 369–382. doi: 10.1016/j.quageo.2011.02.002
- Scholz, D., Mühlinghaus, C., and Mangini, A. (2009). Modelling $\delta^{13}\text{C}$ and $\delta^{18}\text{O}$ in the solution layer on stalagmite surfaces. *Geochim. Cosmochim. Acta* 73, 2592–2602. doi: 10.1016/j.gca.2009.02.015
- Scholz, D., Tolzmann, J., Hoffmann, D. L., Jochum, K. P., Spötl, C., and Riechelmann, D. F. C. (2014). Diagenesis of speleothems and its effect on the accuracy of $^{230}\text{Th}/\text{U}$ -ages. *Chem. Geol.* 387, 74–86. doi: 10.1016/j.chemgeo.2014.08.005
- Sinclair, D. J., Banner, J. L., Taylor, F. W., Partin, J., Jenson, J., Mylroie, J., et al. (2012). Magnesium and strontium systematics in tropical speleothems from the Western Pacific. *Chem. Geol.* 29, 1–17. doi: 10.1016/j.chemgeo.2011.10.008
- Sirocko, F., Knapp, H., Dreher, F., Förster, M. W., Albert, J., Brunck, H., et al. (2016). The ELSA-Vegetation-Stack: reconstruction of landscape evolution zones (LEZ) from laminated eifel maar sediments of the last 60,000 years. *Glob. Planet. Change* 142, 108–135. doi: 10.1016/j.gloplacha.2016.03.005
- Steiger, R. H., and Jäger, E. (1977). Subcommission on geochronology: convention on the use of decay constants in geo- and cosmochronology. *Earth Planet. Sci. Lett.* 36, 359–362. doi: 10.1016/0012-821X(77)90060-7
- Tooth, A. F., and Fairchild, I. J. (2003). Soil and karst aquifer hydrological controls on the geochemical evolution of speleothem-forming drip waters. Crag Cave, southwest Ireland. *J. Hydrol.* 273, 51–68. doi: 10.1016/S0022-1694(02)00349-9
- Treble, P., Shelley, J. M. G., and Chappell, J. (2003). Comparison of high resolution sub-annual records of trace elements in a modern (1911–1992) speleothem with instrumental climate data from southwest Australia. *Earth Planet. Sci. Lett.* 216, 141–153. doi: 10.1016/S0012-821X(03)00504-1
- Treble, P. C., Chappell, J., and Shelley, J. M. G. (2005). Complex speleothem growth processes revealed by trace element mapping and scanning electron microscopy of annual layers. *Geochim. Cosmochim. Acta* 69, 4855–4863. doi: 10.1016/j.gca.2005.06.008
- von Kamp, H., and Ribbert, K. H. (2005). Erläuterungen zu Blatt 4611 Hagen-Hohenlimburg Geologische Karte von Nordrhein-Westfalen 1: 25.000. Krefeld.
- Wanner, H., Beer, J., Bütikofer, J., Crowley, T. J., Cubasch, U., Flückiger, J., et al. (2008). Mid- to Late Holocene climate change: an overview. *Quat. Sci. Rev.* 27, 1791–1828. doi: 10.1016/j.quascirev.2008.06.013
- Warren, S. F., Fohlmeister, J., Schröder-Ritzrau, A., Constantin, S., Spötl, C., Gerdes, A., et al. (2018). Reconstruction of late Holocene autumn/winter precipitation variability in SW Romania from a high-resolution speleothem trace element record. *Earth Planet. Sci. Lett.* 499, 122–133. doi: 10.1016/j.epsl.2018.07.027
- Wassenburg, J. A., Dietrich, S., Fietzke, J., Fohlmeister, J., Jochum, K. P., Scholz, D., et al. (2016a). Reorganization of the North Atlantic Oscillation during early Holocene deglaciation. *Nat. Geosci.* 9, 602–605. doi: 10.1038/ngeo2767
- Wassenburg, J. A., Scholz, D., Jochum, K. P., Cheng, H., Oster, J., Immenhauser, A., et al. (2016b). Determination of aragonite trace element distribution coefficients from speleothem calcite-aragonite transitions. *Geochim. Cosmochim. Acta* 190, 347–367. doi: 10.1016/j.gca.2016.06.036
- Weber, M., Lugli, F., Jochum, K. P., Cipriani, A., and Scholz, D. (2018b). Calcium carbonate and phosphate reference materials for monitoring bulk and microanalytical determination of Sr Isotopes. *Geostand. Geoanal. Res.* 42, 77–89. doi: 10.1111/ggr.12191
- Weber, M., Scholz, D., Schröder-Ritzrau, A., Deininger, M., Spötl, C., Lugli, F., et al. (2018a). Evidence of warm and humid interstadials in central Europe during early MIS 3 revealed by a multi-proxy speleothem record. *Quat. Sci. Rev.* 200, 276–286. doi: 10.1016/j.quascirev.2018.09.045
- Weber, M., Wassenburg, J. A., Jochum, K. P., Breitenbach, S. F. M., Oster, J., and Scholz, D. (2017). Sr-isotope analysis of speleothems by LA-MC-ICP-MS: high temporal resolution and fast data acquisition. *Chem. Geol.* 468, 63–74. doi: 10.1016/j.chemgeo.2017.08.012
- Wedepohl, H. K. (1995). The composition of the continental crust. *Geochim. Cosmochim. Acta* 59, 1217–1232. doi: 10.1016/0016-7037(95)00038-2
- Yang, Q., Scholz, D., Jochum, K. P., Hoffmann, D. L., Stoll, B., Weis, U., et al. (2015). Lead isotope variability in speleothems—A promising new proxy for hydrological change? First results from a stalagmite from western Germany. *Chem. Geol.* 396, 143–151. doi: 10.1016/j.chemgeo.2014.12.028
- Zhou, H., Feng, Y.-X., Zhao, J.-X., Shen, C.-C., You, C.-F., and Lin, Y. (2009). Deglacial variations of Sr and $^{87}\text{Sr}/^{86}\text{Sr}$ ratio recorded by a stalagmite from Central China and their association with past climate and environment. *Chem. Geol.* 268, 233–247. doi: 10.1016/j.chemgeo.2009.09.003

Conflict of Interest: The authors declare that the research was conducted in the absence of any commercial or financial relationships that could be construed as a potential conflict of interest.

Copyright © 2021 Weber, Hinz, Schöne, Jochum, Hoffmann, Spötl, Riechelmann and Scholz. This is an open-access article distributed under the terms of the Creative Commons Attribution License (CC BY). The use, distribution or reproduction in other forums is permitted, provided the original author(s) and the copyright owner(s) are credited and that the original publication in this journal is cited, in accordance with accepted academic practice. No use, distribution or reproduction is permitted which does not comply with these terms.